Cold Atoms & Surface Plasmons

A thesis submitted to the
Department of Physics by
Ng Kia Boon (A0086511J)
in partial fulfilment of the
Degree of Bachelor of Science
with Honours in Physics
2014/2015

Supervisor: Assistant Professor Björn Hessmo

Acknowledgement

I would like to express my heartfelt gratitude to all members of the Björn Hessmo Group, who have given me tremendous support throughout the course of the project, especially my supervisor Asst. Prof. Björn Hessmo, Dr. Paul Condylis, and Ms. Aarthi Dhanapaul, without whom this project would not have been possible. Special thanks go to A/Prof. Kwek Leong Chuan and Mr. Tang Wenjie Shawn, with whom I have had many fruitful discussions with.

Abstract

Attempts were made to construct a plasmonic trap for cold atoms using a prism fabricated with a layer of gold film. This thesis begins with an introduction to the theoretical motivation behind the plasmonic trap, where light polarization and incident angle are identified as critical parameters for successful surface plasmon generation. Attempts were made to detect the plasmonic evanescent through two different methods: (i) optical fibre, and (ii) atomic force microscope (AFM) tip. We showed that the former method is inferior to the latter. Detection of the plasmonic evanescent fields were performed by modulating the incident beam and observing the corresponding modulation on the height of the AFM tip. This is then followed by the investigation of the dependence of the evanescent field strength on the polarization and the incident angle of the incoming beam. We showed that unwanted contribution due to scattering from the surface of a dirty prism is significant enough to drown signals from the plasmonic evanescent fields by comparing results from dirty and clean prisms. The stage has been set for the characterization of the plasmonic evanescent fields for prisms with various gold film grating configurations.

Contents

Chapter 1

Introduction

1.1 Optical Dipole Trap

There are many traps for neutral atoms in existence in addition to optical dipole traps, such as radiation pressure traps, and magnetic traps. There are several advantages to using the optical dipole trap as opposed to its alternatives (Grimm et al., 2000). For example, radiation pressure traps perturb the internal dynamics of the atoms, which limits the variety of internal atomic states that we are free to manipulate; whereas magnetic traps rely highly on the internal states of the atoms, hence not all atoms can be trapped with magnetic traps. The optical dipole trap is free from all the above constraints, but it is the weakest trap of them all. Inasmuch as there are limitations to the optical dipole trap, it still serves as a promising trapping mechanism where alternatives fail.

The size of optical dipole traps is typically bound by the diffraction limit depending on the exact setup configuration. Examples of such configurations include the optical lattice, and the optical tweezers. This limit imposes a lower bound on the size of the traps to the order of the wavelength of the light used. By using evanescent fields as the agent for the optical dipole traps, we overcome the diffraction limit as the length scale that is now involved is the decay length of the exponentially decaying fields, which is on the sub–optical wavelength regime. This allows us to create optical dipole traps which are confined to a much smaller size.

Several authors have already succeeded in realizing various forms of optical dipole traps using evanescent fields. For example, traps have been created using evanescent fields from optical nanofibres (Vetsch et al., 2010), and traps which can be tuned with surface plasmons on a patterned metal surface to suit different purposes have also been realized (Righini et al., 2008). The evanescent fields of surface plasmons have been used in literature for purposes other than for trap creation. These include practical usages like imaging (surface plasmon resonance imaging), and interesting research like the erection of a potential barrier (Stehle et al., 2011, 2013) and the movement of micrometer–sized particles (Kawata and Sugiura, 1992).

The optical dipole trap is well understood, and in this section, I will follow the treatment in Grimm et al. (2000) to derive the dependence of the trap on light intensity and frequency detuning.

1.1.1 Background

The change in energy $\mathrm{d}U$ of a system consisting of an electric dipole $\mathbf{p}$ and a change in electric field $\mathrm{d}\mathbf{E}$ is given by the simple relation:

$$\mathrm{d}U = -\mathbf{p} \cdot \mathrm{d}\mathbf{E}. \tag{1.1}$$

For an electric dipole that varies linearly with the electric field ($\mathbf{p} = \alpha\mathbf{E}$), we then have:

$$\begin{aligned} \mathrm{d}U &= -\alpha\mathbf{E} \cdot \mathrm{d}\mathbf{E} \\ &= -\frac{1}{2}\alpha\,\mathrm{d}E^2. \end{aligned}$$

If we set the energy zero point to be when the field intensity is zero, we have the relation:

$$U = -\frac{1}{2}\alpha E^2 = -\frac{1}{2}\mathbf{p} \cdot \mathbf{E}. \tag{1.2}$$

Equations 1.1 and 1.2 hold at instantaneous instances of time, which would need to be averaged over if the electric field is varying in time to give us an averaged potential energy of the system. This picture of a time–varying electric field applies to a region of space where there is light, as light consists of oscillating electric fields. In complex notation, we expand the time–varying electric dipole and the electric field to:

$$\mathbf{E} = \hat{\mathbf{e}}\left(\tilde{E}e^{-i\omega t} + \tilde{E}^* e^{i\omega t}\right) \tag{1.3a}$$

$$\mathbf{p} = \hat{\mathbf{e}}\left(\alpha\tilde{E}e^{-i\omega t} + (\alpha\tilde{E})^* e^{i\omega t}\right), \tag{1.3b}$$

where $\hat{\mathbf{e}}$ is the polarizing axis of the electric field.

From equations 1.2 and 1.3, we can find the time averaged potential energy $\langle U \rangle$ to be:

$$\langle U \rangle = -\frac{1}{2c\epsilon_0}\,\mathrm{Re}\,(\alpha)\,I, \tag{1.4}$$

where c and ϵ_0 are the speed of light and permittivity of free space respectively, and $I = 2c\epsilon_0\left|\tilde{E}\right|^2$ is the intensity of light[1].

[1]The extra factor of 4 is due to the definitions of $\tilde{E}$ in equation (1.3).

1.1.2 Classical Picture

It is instructive now to take the negative gradient of equation (1.4) to give us the force **F** that the field acts on the electric dipole due to this interaction:

$$\mathbf{F} = -\nabla \langle U \rangle = \frac{1}{2c\epsilon_0} \operatorname{Re}(\alpha) \nabla I. \tag{1.5}$$

We see from equation (1.5) that the electric dipole feels a force that is proportional to the gradient of the intensity of the time–varying field. This prompts us into using intensity gradients as potential barriers or traps for small polarizable things like atoms.

1.1.3 Semiclassical Picture

To wrap up this section, let us take a closer look at the atoms, which require some quantum mechanics for a more accurate picture.

Considering a space with n photons of frequency ω and a two–level system of energy difference $\hbar\omega_0$, with $\omega < \omega_0$, the energy of the ground state of the system is given by:

$$E_g = n\hbar\omega,$$

while that of the excited state is:

$$\begin{aligned} E_e &= (n-1)\hbar\omega + \hbar\omega_0 \\ &= n\hbar\omega - \hbar\Delta, \end{aligned}$$

where $\Delta = \omega - \omega_0$ is the detuning of the photon frequency from the resonant frequency of the two–level system.

We treat one of the photons as a perturbation to the two–level system in the electric–dipole approximation. The first order instantaneous corrections to the energy levels are 0 because:

$$\langle \cdot | -\mathbf{p} \cdot \mathbf{E} | \cdot \rangle = 0$$

due to parity symmetry, and where $\cdot$ refers to either the ground or the excited state.

In the second order corrections, we have, assuming **E** lies in the z-direction:

$$E_i^{(2)} = \sum_j \frac{|\langle i| -\mathbf{p} \cdot \mathbf{E} |j\rangle|^2}{E_i - E_j} = \sum_j \frac{|\langle i| p_z |j\rangle|^2}{E_i - E_j} |E|^2 .$$

Since $\langle i| p_z |j\rangle$ is only non–zero for $i \neq j$, i.e. when i refers to the ground state and j to

the excited state, or the other way round, we obtain:

$$U = E_g^{(2)} \propto \frac{I}{\Delta}, \tag{1.6}$$

where we made use of the fact that $I \propto |E|^2$. The constant of proportionality turns out to be $\frac{3\pi c^2 \Gamma}{2\omega_0^3}$ after some lengthy derivation, where Γ is the on–resonance damping rate. For completeness, we note that:

$$E_e^{(2)} = -E_g^{(2)}.$$

1.1.4 Concluding Remarks

Equation (1.6) can also be derived with the same constant of proportionality through the classical picture from equation (1.5), where we derive the complex polarizability α assuming a damping factor proportional to rate of change of polarizability, and working with the low damping and rotating wave approximations.

One can infer from equation (1.6) that an attractive potential ($U < 0$) can be formed with a red–detuned ($\Delta < 0$) light, and a repulsive potential with a blue–detuned one. The effect of equation (1.6) is nicely summarized in figure 1.1.

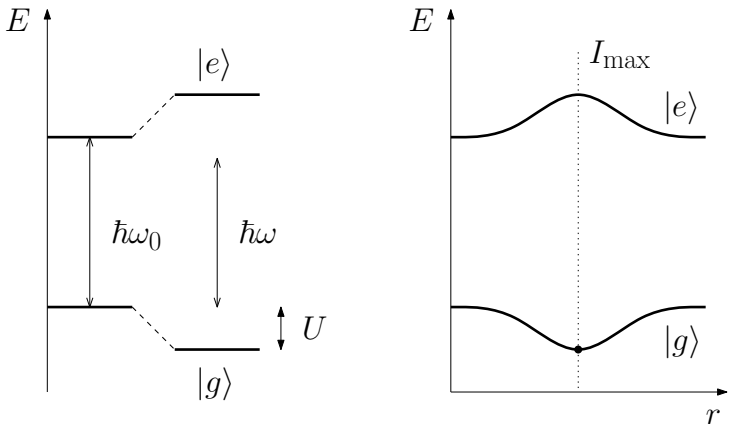

Figure 1.1: Left: Drop (rise) in energy of the ground (excited) state due to the red–detuned perturbation. Right: Change in energy level is greatest where the intensity is greatest.

In this project, I will be working with 780nm light. This will allow us to transit easily to the red and blue–detuned frequencies of the atomic transitions of Rb atoms, which we are hoping to trap as part of the long term goal of this project.

1.2 Surface Plasmons

In this section, I shall follow the treatment in Raether (1988) to demonstrate that surface plasmons (SP) exhibit evanescent fields, which decay exponentially away from the

surface. This will then be followed by a discussion of the conditions required for light–SP coupling.

1.2.1 Background

Light incident on a surface can be characterized by its polarization. For light waves with the electric field parallel (perpendicular) to the plane of incidence, the light is said to be p–polarized (s–polarized). It turns out that only p–polarized light can couple to surface plasmons. For coupling to occur, the $\mathbf{k}$ vectors of both the incoming wave and the surface plasmons must lie in the same plane. Furthermore, the incoming wave can only excite surface plasmons with charges oscillating in the same plane as the polarization axis of the incoming wave. These two conditions only allow p–polarized light to couple to surface plasmons. Figure 1.2 demonstrates the effect that field polarization has on light–SP coupling.

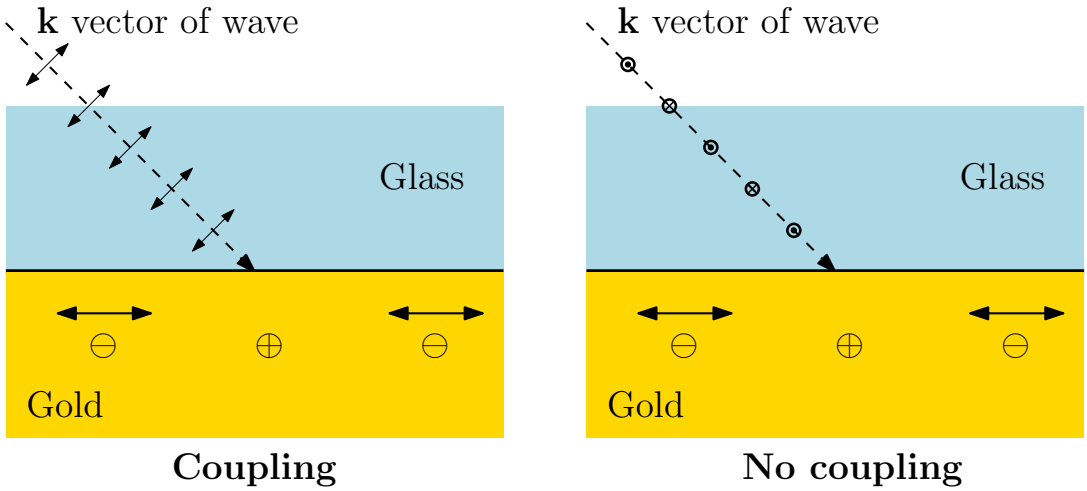

Figure 1.2: Dashed arrow represents $\mathbf{k}$ vector of incoming wave. $\mathbf{k}$ vector of surface plasmons is in the horizontal direction. Left: Electric field is p–polarized; polarization axis, and $\mathbf{k}$ vectors of both the electric field and surface plasmons lie on the same plane, so coupling is possible. Right: Electric field is s–polarized; polarization axis is orthogonal to $\mathbf{k}$ vector of surface plasmon, so coupling is not possible.

Henceforth in this thesis, p–polarization of light is to be assumed in the treatment of all light unless otherwise stated.

For p–polarized electric fields, we rotate our axes such that the electric fields of the surface plasmons lie in the x-z plane as shown in figure 1.3.

As such, the fields for mediums 1 and 2 are given by:

$$\begin{aligned} \mathbf{H}_1 &= H_{y1}\hat{\mathbf{y}} \cdot e^{i(k_{x1}x - k_{z1}z - \omega t)} \quad ; \quad \mathbf{E}_1 = (E_{x1}\hat{\mathbf{x}} + E_{z1}\hat{\mathbf{z}}) \cdot e^{i(k_{x1}x - k_{z1}z - \omega t)} \\ \mathbf{H}_2 &= H_{y2}\hat{\mathbf{y}} \cdot e^{i(k_{x2}x + k_{z2}z - \omega t)} \quad ; \quad \mathbf{E}_2 = (E_{x2}\hat{\mathbf{x}} + E_{z2}\hat{\mathbf{z}}) \cdot e^{i(k_{x2}x + k_{z2}z - \omega t)}, \end{aligned} \tag{1.7}$$

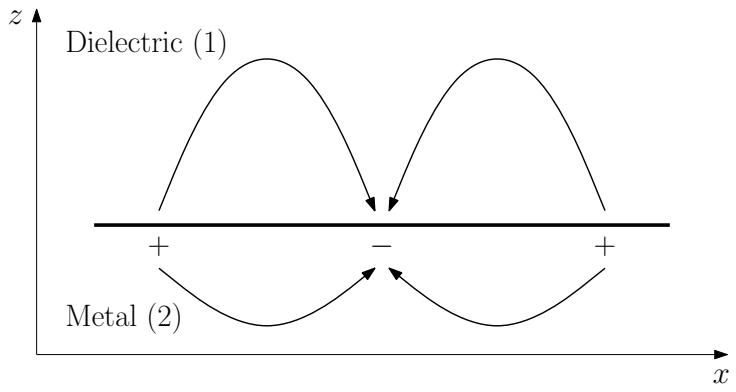

Figure 1.3: Electric field lines lie in the x-z plane. We denote the dielectric and metal as mediums 1 and 2 respectively.

where the k's and ω's take their usual meaning as the wave vector and angular frequency of the oscillating field respectively.

Since there are no free charge or current, we use Maxwell's equations in the form:

$$\nabla \cdot (\epsilon \mathbf{E}) = 0 \quad ; \quad \nabla \times \mathbf{E} = -\mu \frac{\partial \mathbf{H}}{\partial t}$$
$$\nabla \cdot (\mu \mathbf{H}) = 0 \quad ; \quad \nabla \times \mathbf{H} = \epsilon \frac{\partial \mathbf{E}}{\partial t},$$

where ϵ and μ are the permittivity and permeability of the medium respectively, and where we assume that the mediums are linear such that:

$$\mathbf{B} = \mu \mathbf{H} \quad \text{and} \quad \mathbf{D} = \epsilon \mathbf{E}.$$

1.2.2 Boundary Conditions

The fields must match at the boundary where mediums 1 and 2 meet for all x at $z = 0$. This implies the relation:

$$k_{x1} = k_{x2} = k_x. \tag{1.8}$$

We perform an area integral on Faraday's Law over a very small area encompassing the boundary to infer that:

$$\epsilon_1 E_{x1} = \epsilon_2 E_{x2}. \tag{1.9}$$

Similarly for Ampère's Law:

$$\mu_1 H_{y1} = \mu_2 H_{y2}.$$

Since we are not dealing with mediums with permeabilities significantly different from

that of vacuum, we take $\mu_1 \approx \mu_2 \approx \mu_0$ to get:

$$H_{y1} = H_{y2} = H_y. \tag{1.10}$$

1.2.3 Dispersion Relation

Applying Ampère's Law to the component forms of the fields (equations 1.7), we get:

$$\begin{aligned} k_x H_y &= -\epsilon_1 \omega E_{z1} \quad ; \quad -k_{z1} H_y = -\epsilon_1 \omega E_{x1} \\ k_x H_y &= -\epsilon_2 \omega E_{z2} \quad ; \quad k_{z2} H_y = -\epsilon_2 \omega E_{x2}. \end{aligned} \tag{1.11}$$

Combining equations 1.9, and 1.11, we get:

$$\frac{k_{z2}}{\epsilon_2} + \frac{k_{z1}}{\epsilon_1} = 0. \tag{1.12}$$

A similar approach with Faraday's Law on equations 1.7 together with equations 1.8 through 1.11 gives us:

$$k_{zi}^2 + k_x^2 = \epsilon_i \mu_0 \omega^2 \quad , \quad i \in \{1, 2\}. \tag{1.13}$$

Combining equations 1.12 and 1.13 will give us the dispersion relation:

$$k_x = \omega \sqrt{\frac{\mu_0 \epsilon_1 \epsilon_2}{\epsilon_1 + \epsilon_2}} = \frac{\omega}{c} \sqrt{\frac{\varepsilon_1 \varepsilon_2}{\varepsilon_1 + \varepsilon_2}}, \tag{1.14}$$

where $\varepsilon_i = \frac{\epsilon_i}{\epsilon_0}$ is the dielectric constant of medium i.

1.2.4 Evanescent Field

Combining equations 1.13 and 1.14 gives us:

$$k_{zi} = \frac{\omega}{c} \sqrt{\frac{\varepsilon_i^2}{\varepsilon_1 + \varepsilon_2}} \quad , \quad i \in \{1, 2\}. \tag{1.15}$$

Since we have $\varepsilon_2 \approx -24 < 0$ for gold (Johnson and Christy, 1972), which is less than that of the dielectric ($\varepsilon_1 \approx 1$ for air in our case), and that $|\varepsilon_2| > |\varepsilon_1|$, we see that k_z for both mediums turn out to be complex. This means that the fields of the surface plasmons are confined to the surface $z = 0$, and that they decay exponentially as we move away from the surface. We can observe these exponentially decaying fields as the evanescent fields on the dielectric (air) side of the setup.

1.2.5 Light–SP Coupling

The only problem that remains is to couple light with surface plasmons to create them; surface plasmons do not oscillate spontaneously. Earlier on it is mentioned that only p–polarized light can be coupled to surface plasmons. It also turns out that the surface plasmons only couple resonantly to a very narrow range of $\mathbf{k}$ vectors of the incident beam.

The dispersion relations of light in vacuum and surface plasmons are shown in figure 1.4.

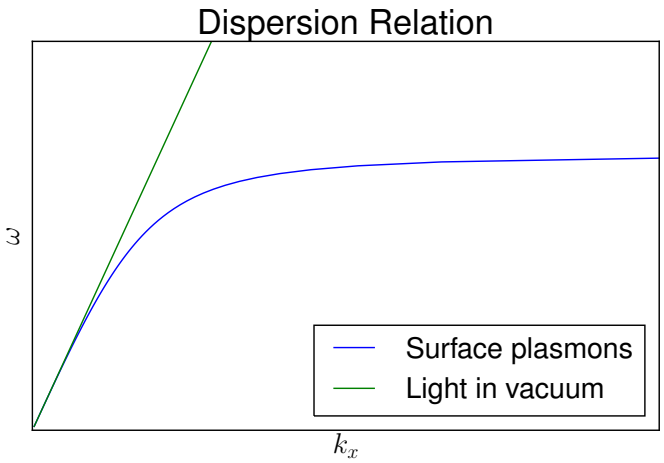

Figure 1.4: Dispersion relations of light in vacuum and surface plasmons. These two lines only intersect when $k_x = 0$. At large k_x, ω for surface plasmons approach $\frac{\omega_p}{\sqrt{1+\varepsilon_1}}$ asymptotically, where ω_p and ε_1 are the plasma frequency and the dielectric constant of the medium respectively.

We see that the two lines only intersect at the origin. This means that light in vacuum has no way to couple to surface plasmons in a non–trivial way. We would like the two lines to intersect at a point where $\omega \neq 0$. This can be accomplished in a number of ways.

Firstly, we can introduce the coupling light through a dielectric, which would slow the light down and reduce the gradient of the light dispersion relation line such that there are now two points of intersection with the surface plasmon line. A typical dielectric medium that can be used is glass (BK7) with a refractive index of 1.51.

Secondly, we can introduce gratings on the metal film. The periodic spacing of a on the gratings will allow coupling to occur between the two dispersion relation lines at ω's where they are separated by $\Delta k = \frac{2\pi}{a}$. Various configurations of gratings on the metal film will allow for more interesting coupling between light and surface plasmons in a similar manner.

Finally, we can combine the aforementioned methods together in various combinations to give us more variations in the coupling of light and surface plasmons. The resultant dis-

persion relations diagrams for the aforementioned methods are summarized in figure 1.5.

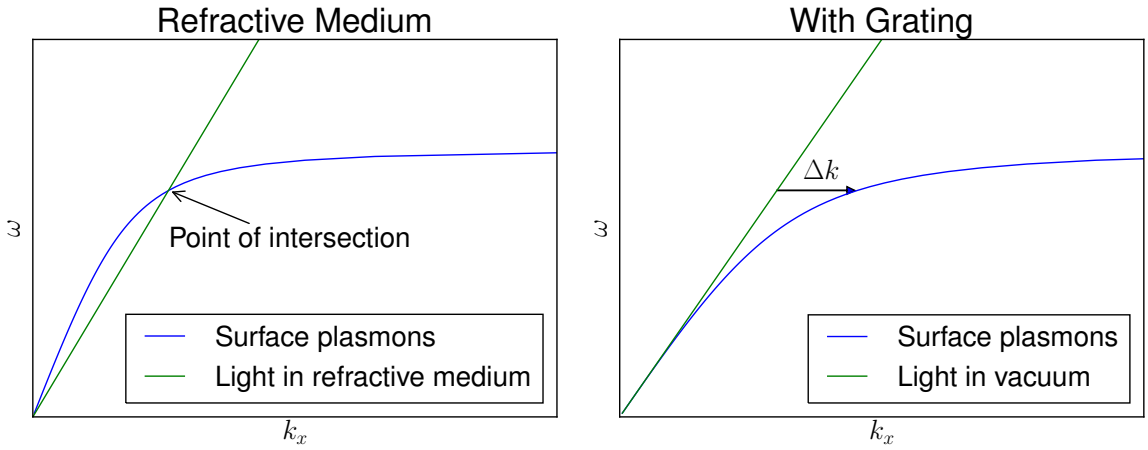

Figure 1.5: Left: Gradient of dispersion relation of light is reduced by introducing the light through a refractive medium, giving a non–trivial point of intersection with the surface plasmon line. Right: Light and surface plasmon coupled through the Δk wave vector, which is introduced by the periodic gratings on the metal film.

1.3 Plasmonic Trap

In this project, both mechanisms mentioned in section 1.2.5 are used together to couple the light with the surface plasmons. The dielectric that was used is glass (BK7), while gold was used as the metal film. Both silver and gold are popular choices in literature for the creation of surface plasmons due to their electrical properties, but gold was chosen over silver because of the comparative inert nature of gold to air in the atmosphere than silver. Since this trap involves the use of surface plasmons, it is sometimes known in literature as the plasmonic trap. Figure 1.6 shows a schematic diagram of the major components in the plasmonic trap.

It is important to note that the laser beam used to couple to the surface plasmon is totally reflected off the inner wall of the glass prism via total internal reflection; there is no refracted beam on the other side of the prism.

From equation (1.6), we infer that a red–detuned (blue–detuned) light will give us an attractive (repulsive) potential. As such, we can create a trap with surface plasmons, i.e. a plasmonic trap, by introducing a blue–detuned and red–detuned light shining onto a metal film. This is summarized by figure 1.7.

From figure 1.7, it is apparent that there is a local minimum in the net potential. This local minimum can then be used as a trap for cold atoms. Using equation (1.15) and substituting the values for air and gold at 780nm light, the decay length to found to

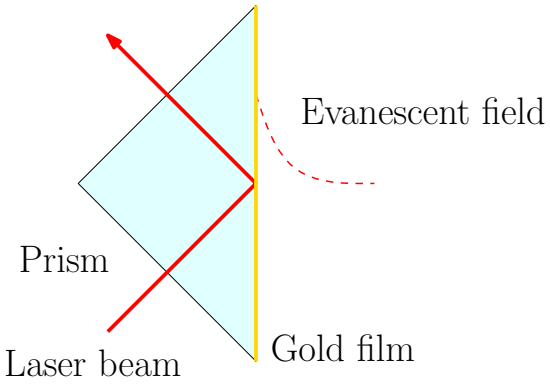

Figure 1.6: Schematic diagram of major components in a plasmonic trap. Laser beam is reflects off inner wall of prism via total internal reflection. Evanescent field intensity dies off exponentially away from surface.

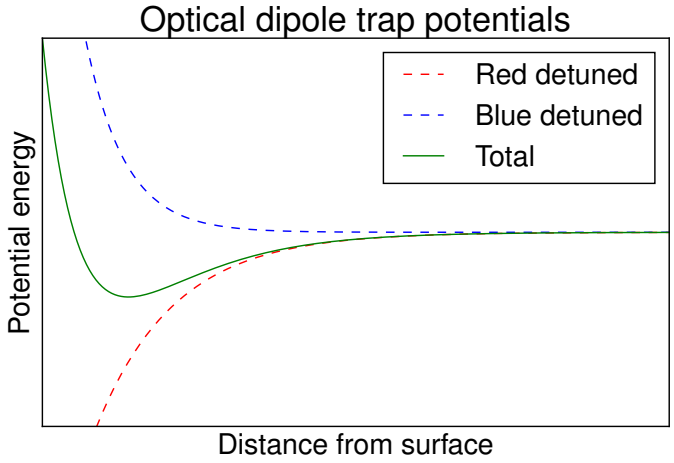

Figure 1.7: Net potential (green line) formed by the superposition of the red–detuned attractive potential and a blue–detuned repulsive potential.

be $\delta = \frac{1}{|k_{z1}|} \approx 160\text{nm}$. This implies that the size of the trap is on the order of 100nm, which is less than the optical wavelength. Hence, we overcome the diffraction limit for the size of the optical dipole trap with the usage of surface plasmons. On a similar note, the length scale of interest for this project is determined by the scale of the decay length, and it is on the order of 100nm to an upper bound of about 1µm.

The exact nature of the traps can be modified by using different grating configurations on the gold film. Therefore, it is worthwhile to put a setup together for the probing of the evanescent fields, which will allow for the characterization of the traps using different grating configurations. The steps taken and the results of the probing are detailed in the next chapter.

1.4 Aims, Motivation & Project Layout

The aim of this project is to create a plasmonic trap for cold atoms. The atoms will be confined to an optical dipole trap manifested by evanescent fields from surface plasmons. Surface plasmons are used as the agents for the optical dipole trap for better trap confinement, as the size of the trap in this configuration is not bound by the diffraction limit.

In this project, I have attempted to detect the plasmonic evanescent fields through a variety of ways in hopes of characterizing the fields for various grating configurations. The fabrication of the various grating configurations on the gold film was performed by a graduate student, Ms. Aarthi Dhanapaul. Although the characterization of the plasmonic evanescent fields was not successfully realized in the course of this final year project, we hope to use this project as a stepping board to implement the plasmonic trap on Rb atoms in the long term.

This thesis shall cover the experimental steps taken to detect and characterize the traps. Chapters 2 and 3 focus on the probing of evanescent fields using an optical fibre and the atomic force microscope as probes respectively. Chapter 4 covers a refinement of the experimental setup of chapter 3 to yield better results. Lastly, we conclude with chapter 5 which summarizes all of the work, and discusses future work that can be done to improve on this current project and to investigate various dependences of the trap properties on the nature of the gratings.

Chapter 2

Field Detection with Optical Fibre

The previous chapter has dealt with the theory and motivation underlying this project. Specific attention has been given to the physics behind the optical dipole trap, surface plasmons, and the plasmonic trap. In this chapter, we will see how the optical fibre is being used to probe the evanescent fields.

2.1 Probe Tip

2.1.1 Setup

One of the main tasks of this project is to detect the evanescent fields of surface plasmons. A typical setup for the detection system is shown schematically in figure 2.1.

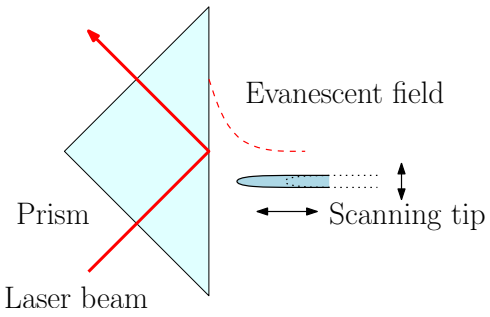

Figure 2.1: Probe tip with 3 translational degrees of freedom, which allows it to perform a depth scan, and an area scan of the evanescent field.

Light is expected to tunnel through the air gap from the prism to the scanning tip. The intensity of the light coupled into the tip can then be detected with a detector on the other end of the fibre. This intensity is proportional to the intensity of the evanescent field at the point where the tip is probing. As such, by measuring the intensity of the light that has tunnelled into the tip at different tip positions, we will be able to deduce the structure of the evanescent field. This forms the core of the detection system.

From figure 2.1, we can immediately recognize an experimental difficulty in the detection of the evanescent field. We note that the laser beam reflects off the inner wall of the prism totally, and this means that there would not be any visual cue to the location of the beam spot on the wall of the prism. Fortunately, this is easily solved by performing an area scan at a constant distance away from the prism to probe for the intensity

maximum, which corresponds to the location of the beam spot. By doing so, we can determine the exact location of the beam spot, where the detection and characterization of the evanescent fields can be performed.

A setup was constructed using Nufern 780-HP bare optical fibre, piezo stages, photo–detector, and the relevant optical components. A schematic diagram is shown in figure 2.2.

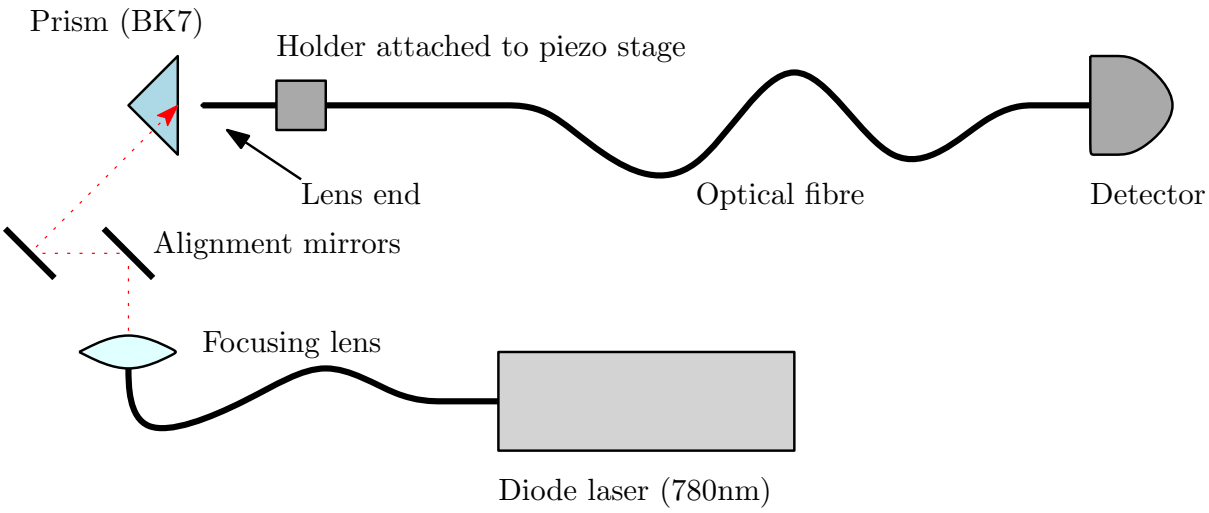

Figure 2.2: Laser beam at 780nm is directed into the prism for total internal reflection. An optical fibre with a lens end is used as a probe tip by attaching it to piezo stages for translation in all three directions.

The bare optical fibre was melted at one end to form a lens. This gives a more defined tip for a more controlled probing of the evanescent fields as compared to an optical fibre with jagged cut edges.

A pre–amplified photo–detector was used as the detector on the other end of the optical fibre. The readings were sent to a computer.

I have written a simple program in *LabVIEW* to coordinate the scanning of the piezo stage and the collection of the data from the photo–detector. With this program, depth scans can be performed to map out the exponential decay of the intensity, and area scans can be performed to locate the beam spot. The beam diameter is at about 1mm.

2.1.2 Absolute Displacement

Since the decay length is sub–optical wavelength at about 100nm as previously stated, there could be no visual cue to the tip–prism distance at the distance scale of interest. Hence, the depth scan was started with the tip in contact with the prism.

Contact was deemed to be made when the fibre was clearly seen to have a slight bend due to the prism wall and fibre holder pushing onto the fibre. The tip would then be retracted with a micrometer screw until it straightens. The scans would start from there.

Before this method is perfected, a glass prism without the gold film is used to prevent unnecessary damage to the precious gold film.

The above method proves to be a problem in a number of ways. Firstly, this is not a reliable method to ensure that scans begin at the same starting point as the micrometer screw does not account for the sub–micron length scales which are involved in this setup. Secondly, the starting points of the scans are determined in a rather subjective manner. Lastly and more importantly, residues were observed on the surface of the prism after a couple of scans. Figure 2.3 shows images of the residues on the glass prism.

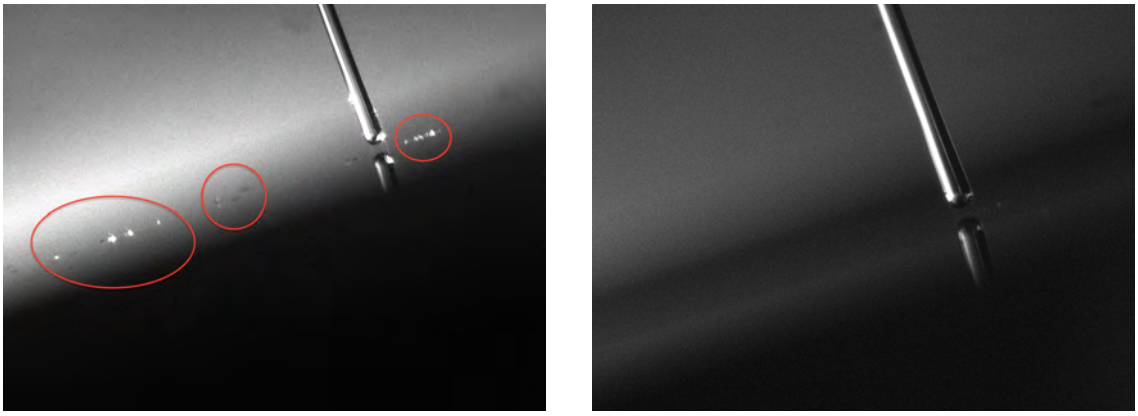

(a) Residues (red circles) **(b)** Prism after blowing with air gun

Figure 2.3: Scattering of light from residues observed on prism along line of scan. Reflection of the scanning tip can also be seen in the images.

There are a number of reasons for the sighting of the residues. Firstly, it is noted that the prism is not aligned exactly parallel to the axes of the piezo stage, hence an area scan of the prism surface with a tilted prism would result in the tip dragging along the surface at some point (refer to figure 2.4). This could induce scratching.

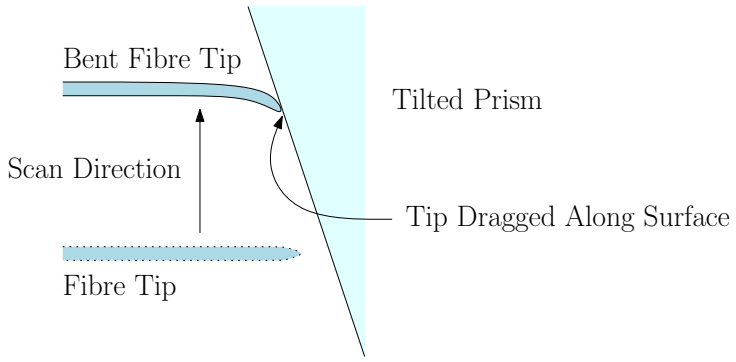

Figure 2.4: Schematic diagram showing the effect of the tilt of the prism on the scan.

Furthermore, since the residues happen to appear in a line corresponding to a lateral translation for the piezo stage, it can be deduced that these residues could be scratch residues from the optical fibre.

Secondly, since the setup was exposed to open air, these residues could be dust particles which have accumulated on the fibre tip, which then was conveniently wiped onto the prism during the scan during the tip–prism contact.

It turns out that scattering from aforementioned residues made the detection of evanescent fields impossible as it drowns the weak evanescent signals with the relatively strong scattered light. This gives rise to multiple "false positives" for the location of the beam spot in the area scan. An image of a "false positive" is shown in figure 2.5.

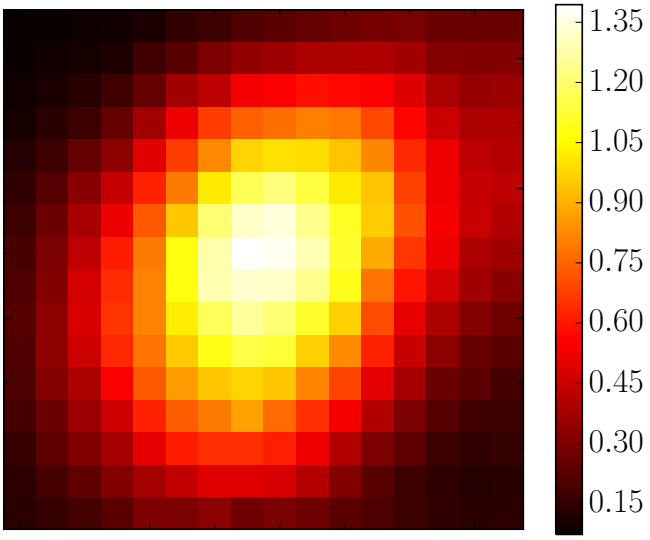

Figure 2.5: Sample intensity mapping of a "false positive". This is a 16×16 pixel–square for an 8×8 micron–square scan. The colour bar is in units of volts, which corresponds to the detected intensity.

2.1.3 Remarks

The above observations prompt the need to implement a feedback system to ensure that the tip can be kept at a constant and non–zero distance away from the prism surface. This will prevent tip–prism contact and unpleasant events like scratching from taking place.

2.2 Primitive Feedback System

2.2.1 Setup

A feedback system proposed by Dr. Paul Condylis involves the use of a probe beam. A beam would be sent through the optical fibre towards the prism, whereupon Fresnel's equations dictate that about 4% of the incident beam would reflect, and some of it

would couple back into the fibre. The coupling strength would be tip–prism distance dependent. The intensity of the reflected beam that is detected on the other side of the fibre is expected to be strong (weak) when the tip is close to (far from) the prism surface. Hence, we would expect to see a decaying intensity as the tip is moved away from the surface. Using this approach, the piezo stage can be adjusted to move in the longitudinal direction such that the intensity of the reflected probe beam is held constant through the feedback system. This would keep the tip at a constant distance away from the prism surface.

This system would require the setup to have a detection system that can switch between the detection of relatively strong reflected probe beam ($\sim$1mW) and relatively weak evanescent fields ($\sim$1pW). This is done by introducing two detectors for the two regimes. A schematic diagram of the setup is shown in figure 2.6.

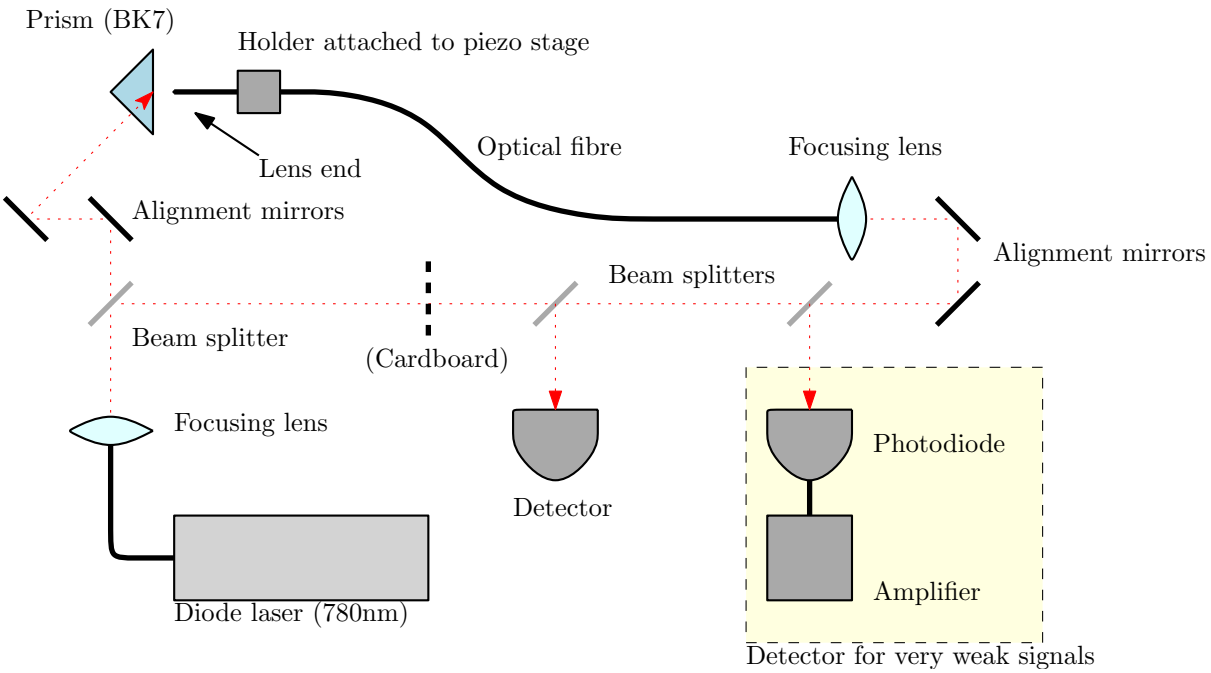

Figure 2.6: Probe beam is sent into the optical fibre, which reflects when it hits the glass prism and couples back into the fibre. The reflected beam is picked up by a pre–amplified photodetector. A piece of cardboard is used to chop the probe beam when the longitudinal coordinate is fixed, and the evanescent fields would be detected with the photodiode detector.

The detector used for the reflected probe beam is the same detector used in section 2.1, and the detection system for weak signals consists of a silicon photodiode and an SRS70 current amplifier.

The tip of the optical fibre was first designed to be flat for easier theoretical analysis of the coupling of the reflected probe beam into the fibre.

2.2.2 Detection Scheme

The proposed evanescent field detection scheme involves an area scan to locate the beam spot. At each point of the area scan, the piezo stage is adjusted longitudinally to lock on to a pre–determined intensity of the reflected probe beam. Once locked, the probe beam would then be chopped off by the piece of cardboard, and a reading would be taken by the detector for the evanescent fields. Once the system proves to work, the chopping of the beam could be automated at a later stage.

2.2.3 Results of the System Test

Little could be done with this new feedback system as it was soon found out that the intensity of the reflected probe beam did not vary in the way that was hoped. Depth scans were performed starting at an arbitrarily small tip–prism distance. The *LabVIEW* program was used to coordinate the scan and data collection. A sample plot of the intensity of the reflected probe beam against relative displacement of the tip is shown in figure 2.7.

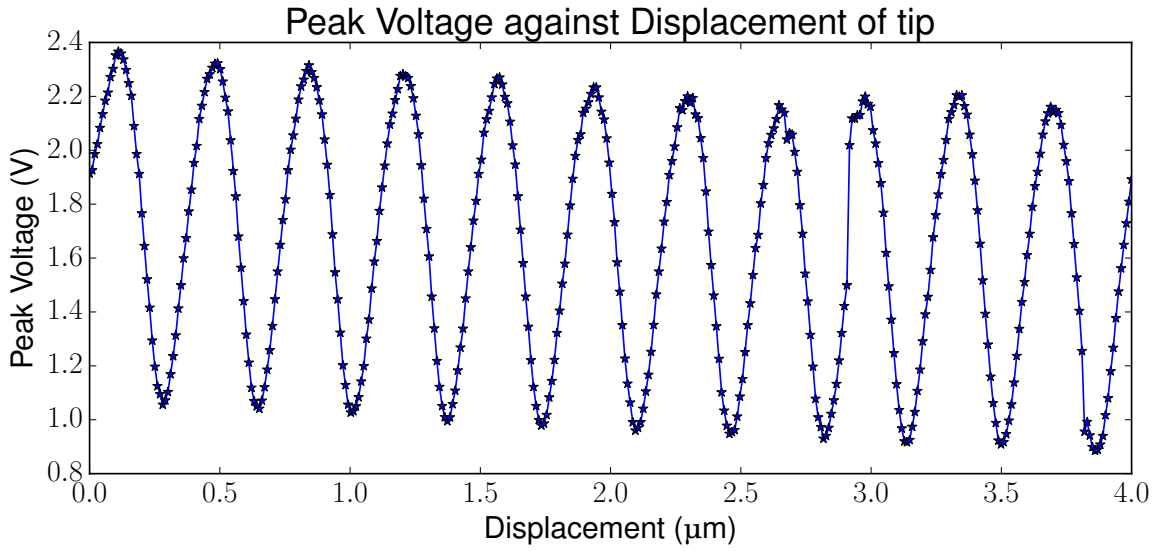

Figure 2.7: Plot of the intensity of the reflected probe beam (in arbitrary units of voltage) against relative displacement of the probe tip. Uncertainty for the peak voltage values is 0.005V, which is attributed to half the smallest digit for the reading; uncertainty for the displacement is 10nm, which is attributed to the resolution of the piezo drivers.

Figure 2.7 shows that the intensity of the reflected probe beam varies sinusoidally with a decreasing moving average with increasing distance from the prism surface. The sinusoidal variation is attributed to the Fabry–Pérot etalon that is formed by the prism surface and the optical fibre. Since the length scale of interest to us is the region below

1 micron, we note from figure 2.7 that there is little variation in the moving average of the intensity within that length scale, i.e. the envelope is not varying fast enough for the intensity to look drastically different for points separated by 1 micron. In mathematical terms, the peak voltage is not a bijective function of the displacement; each peak voltage value does not correspond to a unique displacement value. Hence, we would not know the actual tip–prism displacement given the intensity at a point. Further investigation shows that the decaying envelope does not display a clear trend which can be replicated on every scan site. This indicates the decay is highly dependent on the exact coupling nature of the reflected light and the probe tip. Since the prism surface and tip are not well characterized, little could be done to fix this.

2.2.4 Remarks

This feedback system allows the fibre tip to lock onto an approximately fixed distance by virtue of the sinusoidal variation of the intensity due to the etalon effect. This solves the scratching and contact problem as mentioned in section 2.1. However, since it tells us little about the absolute tip–prism distance, we would have little idea as to whether the tip is even close enough to the prism surface for the detection of the evanescent fields. As such, a new feedback mechanism is needed.

2.3 Summary

In this chapter, we have seen how the optical fibre can be used to probe the evanescent fields. We have also seen how a feedback system can be implemented to ensure a constant tip–surface distance. However, the actual implementation turns out to be much harder than expected. We have seen the ill effects of the tip being dragged along the prism surface, and we have seen that it is not easy to position the optical fibre tip reliably close enough to the prism surface for the evanescent field detection. This prompts the need for a feedback mechanism that can (i) ensure constant tip–surface distance, and (ii) ensure that the tip is close enough to the surface for the evanescent fields to have an effect on the tip. This new feedback system will be covered in the next chapter.

Chapter 3

Field Detection with Atomic Force Microscope

In the previous chapter, we have seen how the optical fibre is not a good probe for the detection of the evanescent fields due to a variety of reasons discussed. In this chapter, we will see how the atomic force microscope (AFM) is a better probe for the evanescent field detection.

3.1 Atomic Force Microscope Feedback System

3.1.1 Setup

I have adapted an atomic force microscope (AFM) to function as the probe tip and feedback system concurrently. A similar approach using the scanning tunnelling optical microscope has been done by Marti et al. (1993). A schematic diagram of the setup using AFM is shown in figure 3.1.

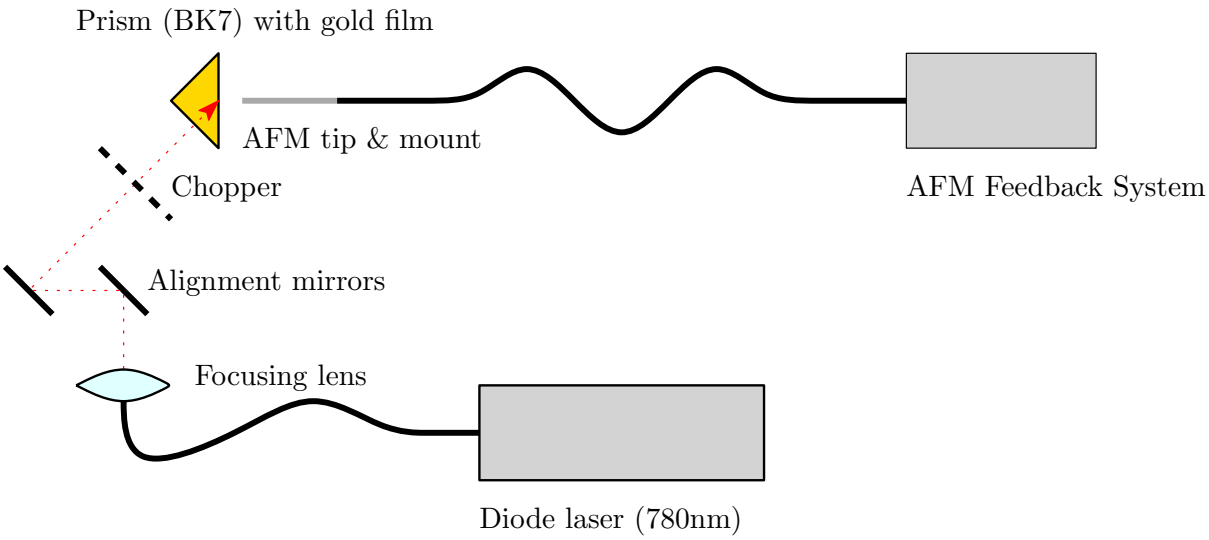

Figure 3.1: An AFM is used as both the probe tip and the feedback system to maintain constant tip–prism distance.

Some pictures of the setup is shown in figure 3.2. The AFM system and the accompanying software, *MultiView 2000*, was provided by *Nanonics*. A steel bracket was specially

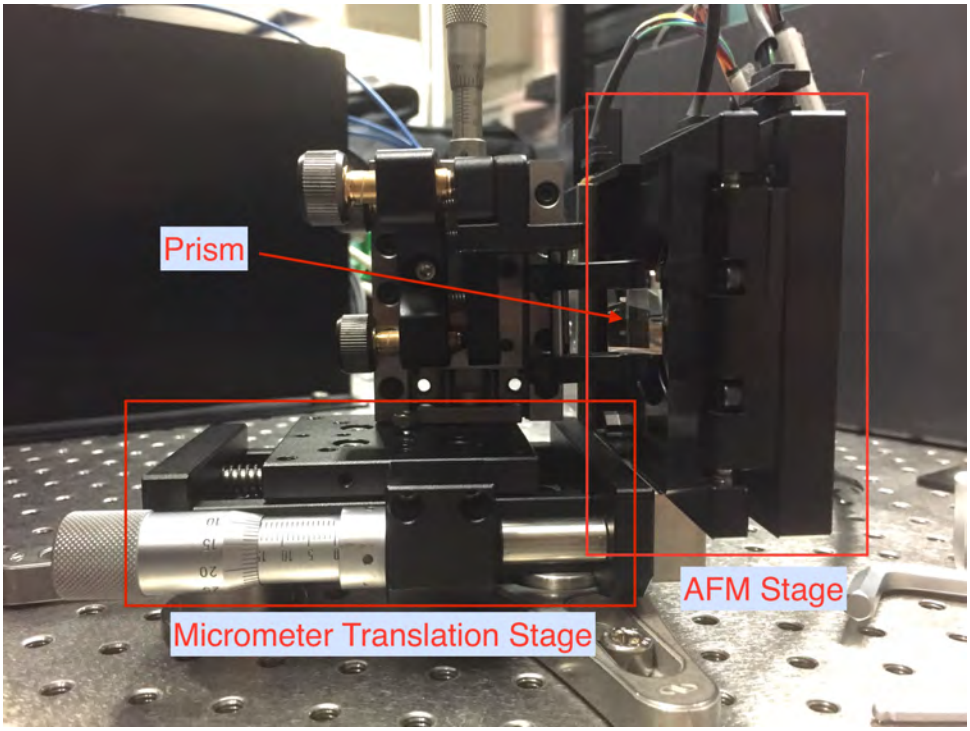

(a) Side view: AFM stage is flipped sideways and mounted on a micrometer translation stage.

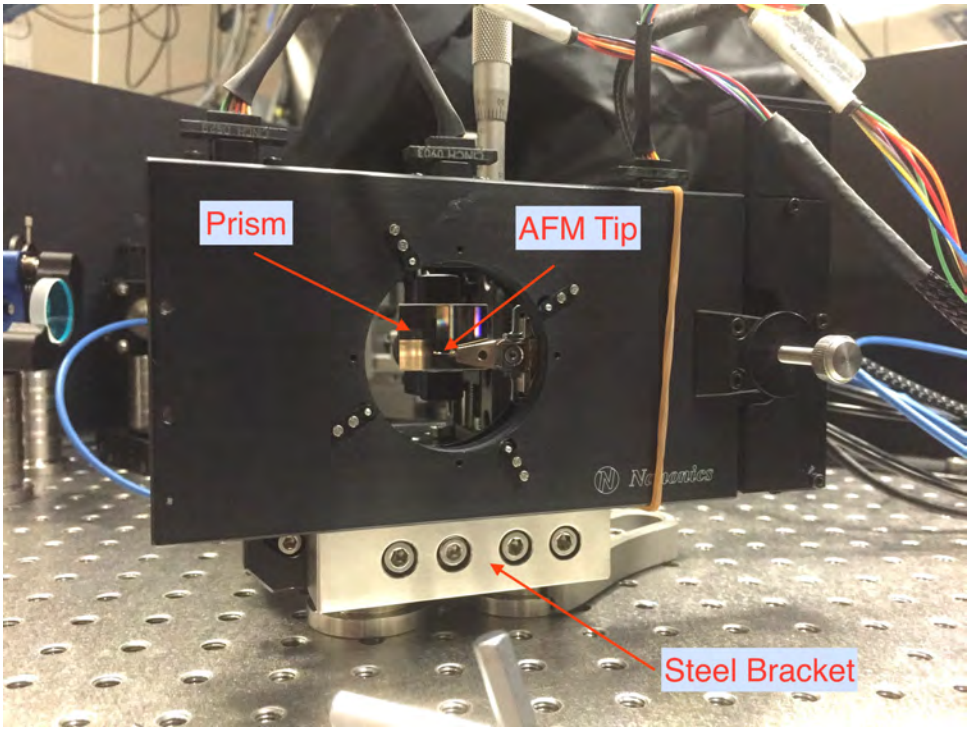

(b) Front view: AFM tip and front face of prism can be seen. The glass and gold coated halves can be seen. Steel bracket can be seen attached to the micrometer translation stage.

Figure 3.2: Steel bracket used to mount AFM to micrometer translation stage. The lower stage of the AFM has been removed in this adaptation.

designed to mount the AFM stage onto a platform with the prism. The lower scanning stage of the AFM has been removed for wider access of the prism for the AFM tip in this setup configuration. A prism with a thin gold film ($\sim$ 100nm thick) coated on the lower half of its surface is used. Comparisons of the evanescent fields due to the bare glass in the upper half of the prism and the plasmonically enhanced fields due to the surface plasmons on the lower half can then be made easily by moving the prism with a translation stage.

At this stage, it serves to go into the mechanics of the AFM to explain how the AFM can be used to detect the plasmonic evanescent fields before I go into the detection scheme using the AFM.

3.1.2 AFM Mechanics

The AFM tip is mounted on a tuning fork (Binnig et al., 1986; Butt et al., 2005; Nanonics, 2010), which oscillates at a resonant frequency determined by calibration. The amplitude of the tuning fork oscillation is first scanned across a range of frequencies to obtain a plot as shown in figure 3.3. From the plot, we infer the resonant frequency and configure the AFM software to lock on to that frequency.

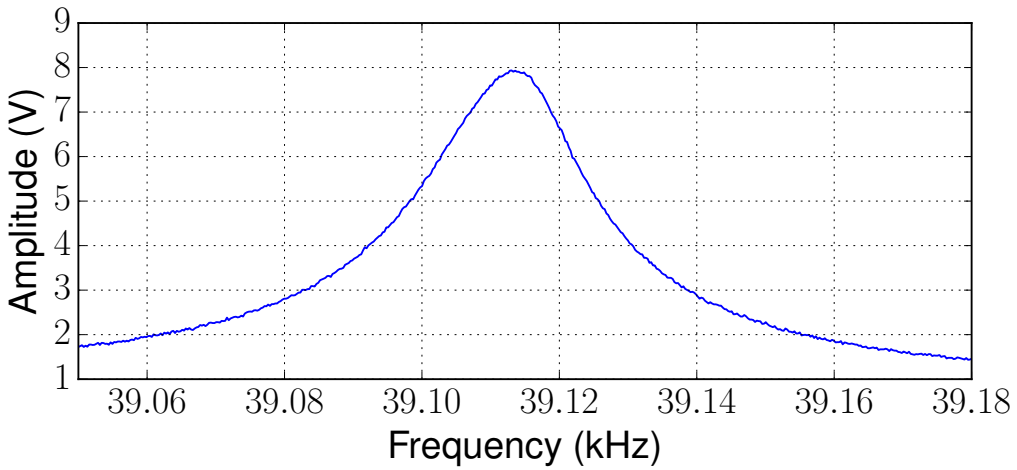

Figure 3.3: Plot of amplitude of the tuning fork oscillation against oscillation frequency. The position of the peak corresponds to the resonant frequency. Resonant frequency in this plot is 39.113kHz.

Once the above calibration is done, we can proceed on with the scan. As the tip approaches the surface, surface forces like the van der Waals force begin to take effect. To illustrate the effects of the surface force, I will assume that the van der Waals force is the most dominant surface force in the following discussion, from which it can be easily generalized to any arbitrary surface force.

The van der Waals force between a flat surface and a cone is given by (Butt et al., 2005):

$$F = -\frac{A_H \tan^2\theta}{6D},$$

where A_H is the Hamaker constant that determines the coefficient of the force, θ is the angle of the cone, and D is the cone–surface distance. Since $F = -\frac{\mathrm{d}U}{\mathrm{d}D}$, we see that together with the harmonic potential of the tuning fork, the tip sees an effective potential of:

$$U(D) = \frac{1}{2}m\omega^2(D - D_0)^2 + \frac{A_H \tan^2\theta}{6}\ln D, \tag{3.1}$$

where D_0 is the equilibrium position of the tip, i.e. the height of the tip.

Performing a Taylor series expansion of equation (3.1) about D_0 and including terms up to second order in $(D - D_0)$ only, we see that:

$$U(D) \approx \left[\frac{1}{2}m\omega^2 - \frac{A_H \tan^2\theta}{12D_0^2}\right](D - D_0)^2 + \frac{A_H \tan^2\theta}{6}\ln D_0 + \frac{A_H \tan^2\theta}{6D_0}(D - D_0).$$

From the above equation, we can infer that the resonant frequency of the tuning fork is shifted under the influence of the van der Waals force to become tip–surface distance dependent:

$$\omega'^2 = \omega^2 - \frac{A_H \tan^2\theta}{6mD_0^2}.$$

The AFM detects the change in resonant frequency of the tuning fork, and tries to move the tip up to reduce the effects of the van der Waals force such that the resonant frequency stays slightly below the predetermined frequency set during the calibration phase. A PID feedback system controls how much the tip moves when the resonant frequency has been changed by a certain amount.

As the AFM performs an area scan, the PID system tries to keep the tip at a constant tip–surface distance as it locks on to that predetermined frequency. As such, by reading out the height of the tip at each point of the area scan, we will be able to map out the topography of the surface.

3.2 Field Detection

3.2.1 Detection Scheme

By introducing the evanescent fields, an additional optical dipole force will be induced on the tip. This effectively modifies the surface forces, and the height of the tip has to be adjusted by the AFM system to keep the force acting on the tip to be a constant. Therefore, by modulating the evanescent field with a chopper at a known frequency, a modulation of the tip height at the same frequency would indicate the presence of the evanescent fields.

3.2.2 Problem with New Stage Orientation

The AFM is usually used with the stage placed parallel to the ground instead of the rotated orientation as discussed above and shown in figure 3.2. It turns out that the AFM has malfunctioned upon flipping it over to this new orientation.

The AFM performs its area scan by scanning each line in the area twice, once in the forward direction and once backward. The forward scan is known as the *trace*, while the backward scan is known as the *retrace*. Figure 3.4 shows a schematic diagram of what the scan path looks like.

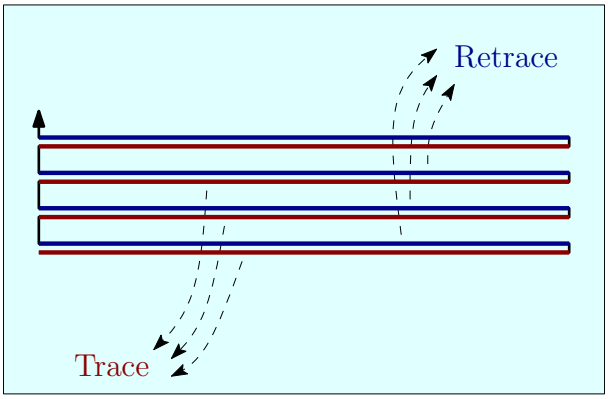

Figure 3.4: Schematic diagram of a typical scan path. The spatial separation between trace and retrace of the same line, which is supposed to be zero, is exaggerated for this illustrative purpose.

It turns out that area scans exhibit significant hysteresis for each of the line scans in this new orientation, i.e. the trace and retrace do not correspond to the same line of the scan sample. A comparison of the trace and retrace scans are shown in figure 3.5. These images are extracted from the raw scan results using a free software: *Gwyddion*.

Sample images of the AFM prior to setting it up in its new orientation are shown in figure 3.6 for comparison with figure 3.5. These scans were performed in the starting

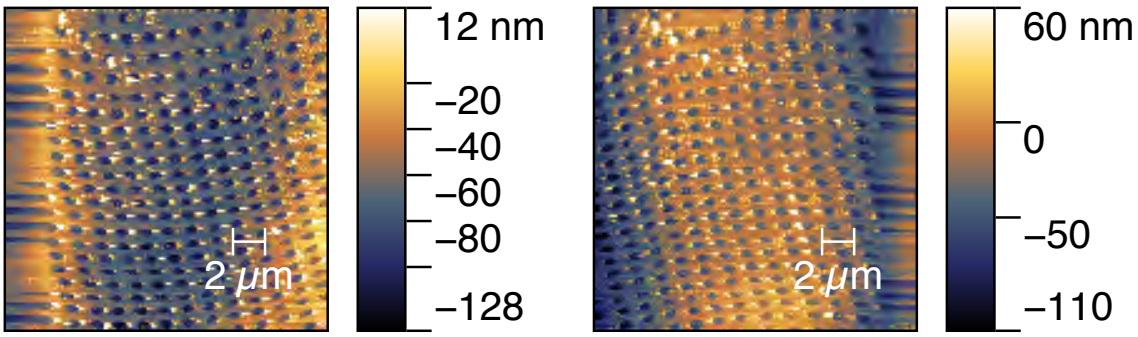

(a) Trace **(b)** Retrace

Figure 3.5: Results of the same scan for both trace and retrace on a calibration chip with holes spaced at regular intervals in a square lattice configuration. Both images should look identical in the ideal situation. Severe distortion and warping of the area scan can be readily seen in both images.

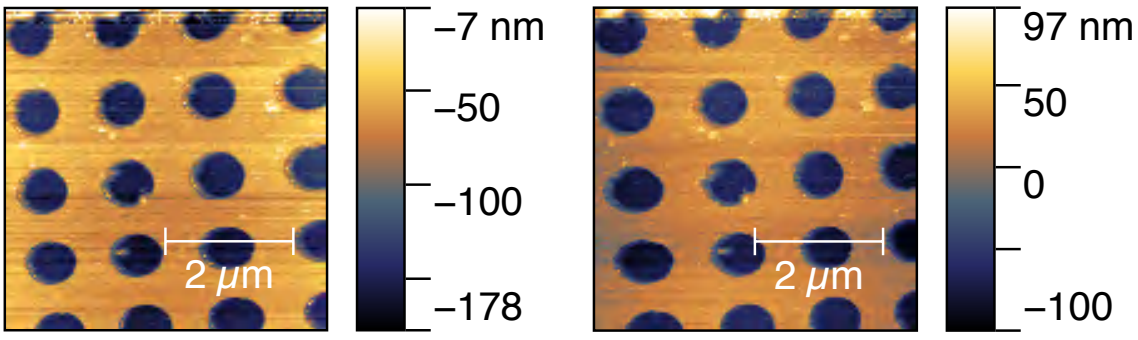

(a) Trace **(b)** Retrace

Figure 3.6: Results of the same scan for both trace and retrace on a calibration chip with holes spaced at regular intervals in a square lattice configuration. The trace and retrace look almost identical. These scans were performed in the starting weeks of this project to familiarize with the AFM instrument, and also for instrument calibration.

weeks of this project for instrument familiarization and calibration. The scans in figure 3.6 are also of the same calibration chip used in figure 3.5. We see minimal distortion and warping of the area scans, and we also see that the trace and retrace look almost identical to each other.

The distortion and warping problem is not rectified upon returning the AFM stage to its usual orientation. It is possible that the scanning components in the AFM have loosened in the process of mounting the AFM stage in its new orientation. To prevent further deterioration, the setup was reorientated such that the scanning stage is parallel to ground. The optics have also been adapted accordingly. The setup is shielded with foam (mattress from *IKEA*) from acoustics in the lab as the AFM is very sensitive to ambient noise. Sample images of the setup are shown in figure 3.7.

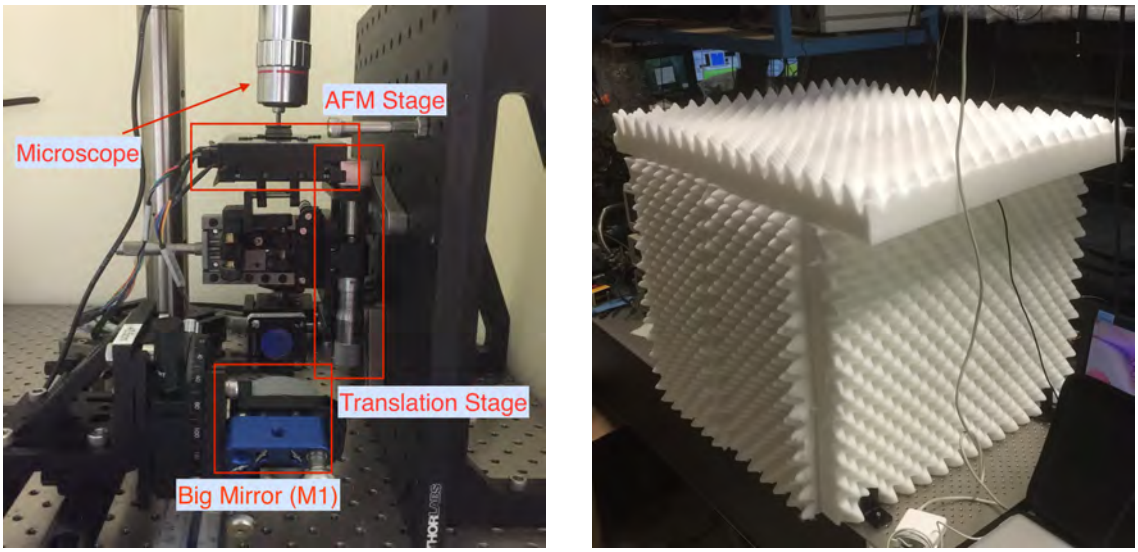

(a) Reorientated AFM stage. **(b)** Setup shielded by foam.

Figure 3.7: Sample images of the setup. Microscope acts as a visual aid for the scanning area. Foam shields whole setup from ambient acoustics. The big mirror shall be referred to as M1 from now on.

The incident angle at which the laser hits the inner wall of the prism is controlled by the rail–mirror system, which can be seen in figure 3.7. This rail–mirror system consists of a big mirror (referred to as M1 from now on), which is attached to a rotating platform on a set of parallel rails. By varying the translational position and the angle of M1, the incident angle can be changed accordingly while keeping the beam spot position fixed. A polarizing beam splitter and half wave plate system ensures that the incoming laser beam is linearly polarized. It has been checked that M1 does not introduce significant circular polarization. A schematic diagram of the rail–mirror system is shown in figure 3.8.

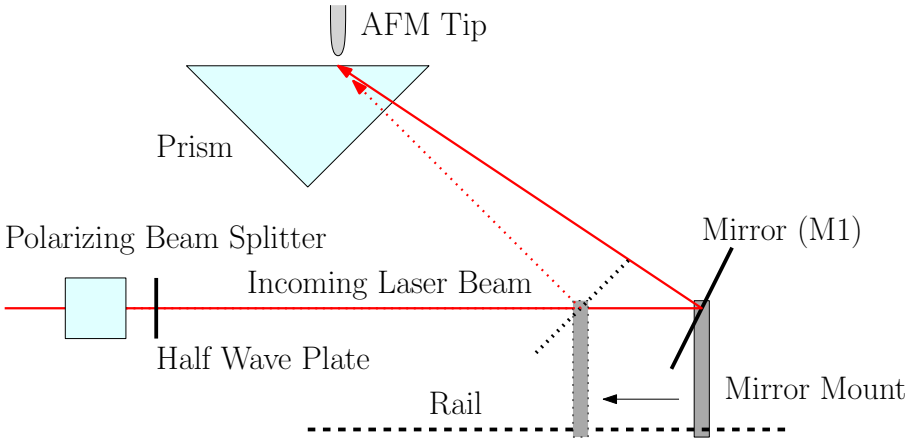

Figure 3.8: Side view of the rail–mirror system. Used to control the incident angle of the laser beam onto the inner wall of the prism. The refraction of the ray as it enters the prism is not drawn to prevent clutter of the diagram. The polarizing beam splitter and half wave plate system ensures that the incoming laser beam is linearly polarized.

3.2.3 Field Detection

By moving M1 around, the critical angle of the prism was found, and attempts were made to detect the evanescent fields. Since the angle at which there is maximum light–SP coupling is about 1° away from the critical angle (Stehle et al., 2011), M1 was adjusted through 1°, which corresponds to approximately 1.5° in range of incident angle from the critical angle, at intervals of 5 arc minutes for each detection attempt. Correlation between the AFM tip height and the modulation of the laser beam was not observed.

3.2.4 Setup Modification

The unexpected lack of correlation between the AFM tip height and the modulation of the laser beam could be due to the power of the laser beam begin insufficient to induce detectable plasmonic evanescent fields. As such, I have made several modifications to the setup to tackle this problem: (i) the beam was focused using an achromat lens to a beam diameter of 150µm from the previous 4mm; (ii) the power of the beam was increased to 15mW from the previous 5mW; (iii) instead of modulating the beam with a chopper, I now modulate the laser diode current controller directly. The last modification allows modulation of the beam to be performed with a much lower frequency, which was limited by the chopper setup due to restrictions set by the equipments.

The above steps in setup modification prove to be useful, as correlation between the AFM tip height and the modulation of the laser beam begin to surface. M1 was kept at the critical angle for these scans. A *LabVIEW* program was written to collect the data. The data was collected at 1000 samples per second. A sample plot of the modulation and height output voltages from the AFM is shown in figure 3.9.

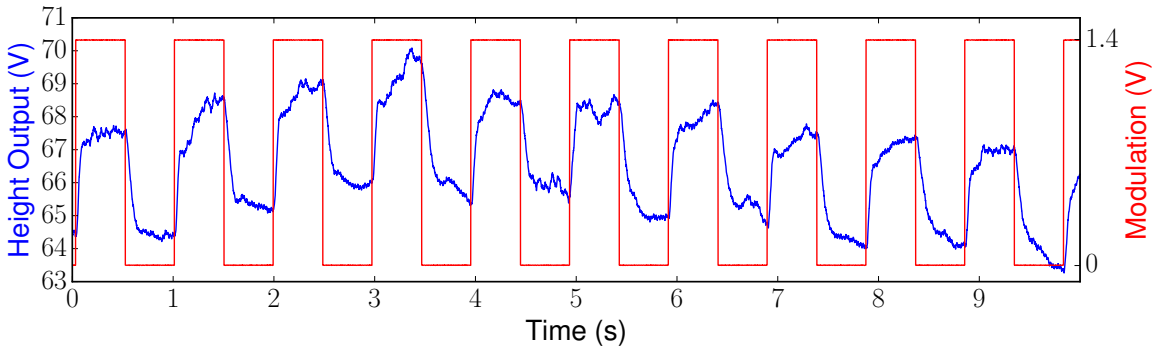

Figure 3.9: Modulation signal (in red) and height output of AFM tip (in blue) plotted together. We see correlation between the two amidst the noise in the AFM height output signal. This scan was done with the tip above the gold film. Uncertainty in height output signal is 0.005V, which is attributed to half the smallest digit of the reading.

We would expect scans over the bare glass surface to have a much less discernible correlation due to the lack of plasmonic enhancement of the evanescent fields by the gold foil. Indeed, we do observe this drop in contrast. In fact, the contrast is lost to the noise of the scan. A sample plot of a scan over glass is shown in figure 3.10.

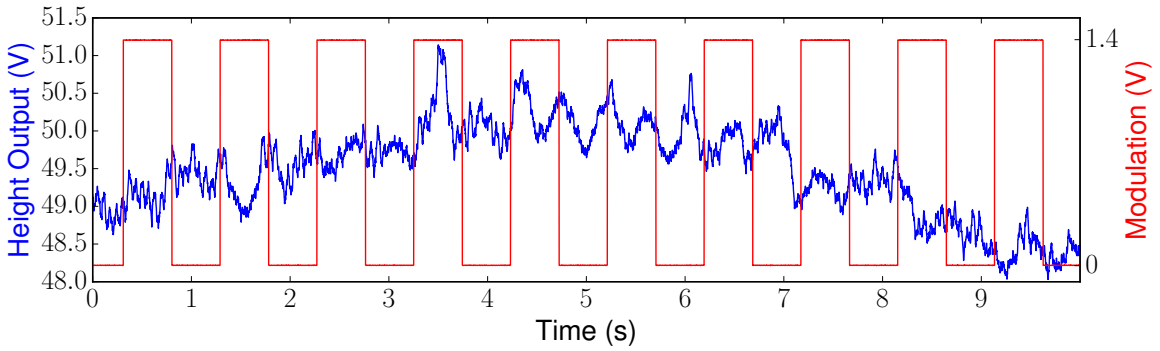

Figure 3.10: Modulation signal (in red) and height output of AFM tip (in blue) plotted together. We do not see correlation between the two; contrast is possibly lost in the noise. This scan was done with the tip above the bare glass surface. Uncertainty in height output signal is 0.005V, which is attributed to half the smallest digit of the reading.

Since Stehle et al. (2011) have calculated the plasmonic enhancement factor to be about 14, we see that a variation of 4V in the height output voltage due to the modulation for the gold scan would give about 0.3V for the glass scan, which would be easily drown by noise.

A discrete Fourier analysis is performed, and figure 3.11 shows the Fourier decomposition of the modulation voltage, height output voltages for the gold and glass scan.

A simple comparison can easily convince us that there is indeed correlation between

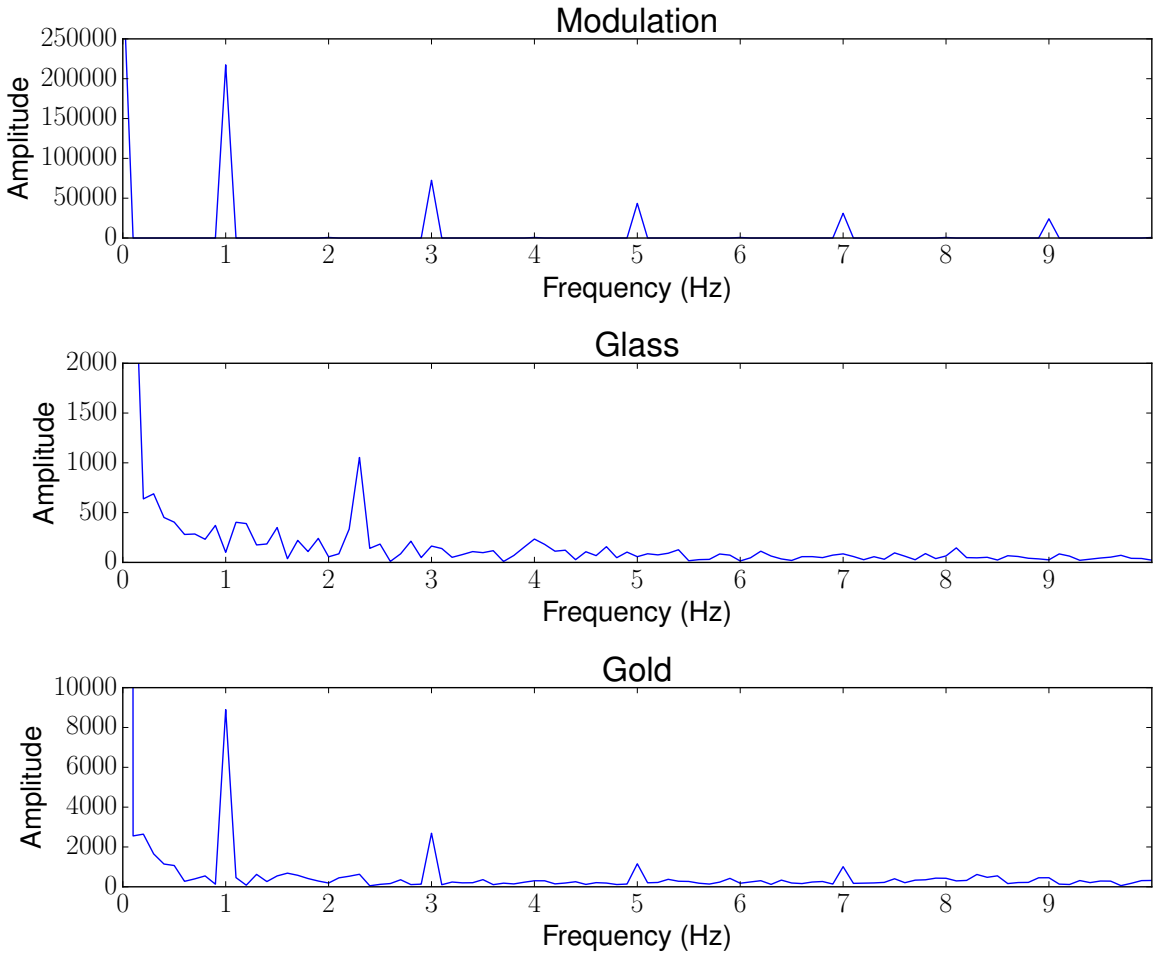

Figure 3.11: Top: Fourier decomposition of the modulation signal. Middle: Fourier decomposition of the height output of the glass scan; does not look like the top plot at all. Bottom: Fourier decomposition of the height output of the gold scan; has the general features of the top plot. In all above plots, the amplitudes plotted are the magnitude of the Argand vector for the corresponding frequency.

the modulation signal and the height output of the gold scan, but that the correlation is masked by noise for the glass scan. The peak at 1Hz and its even harmonics are reminiscent of the 1Hz square–wave modulation used for the scans.

3.3 Analysis of Results

3.3.1 Optimized PID Settings

Figure 3.9 shows a height output profile that seems to have slow convergences. This could be attributed to the unoptimized PID gain settings of the AFM. The overall drift in the height output is attributed to thermal drifts within the setup. However, despite efforts to optimize the PID gain settings, I have only managed to introduce a steeper climb and drop at the instances where the modulation signal changes; slopes of non–negligible gradients can still be observed. Figure 3.12 compares figure 3.9 with that using an optimized PID gain setting.

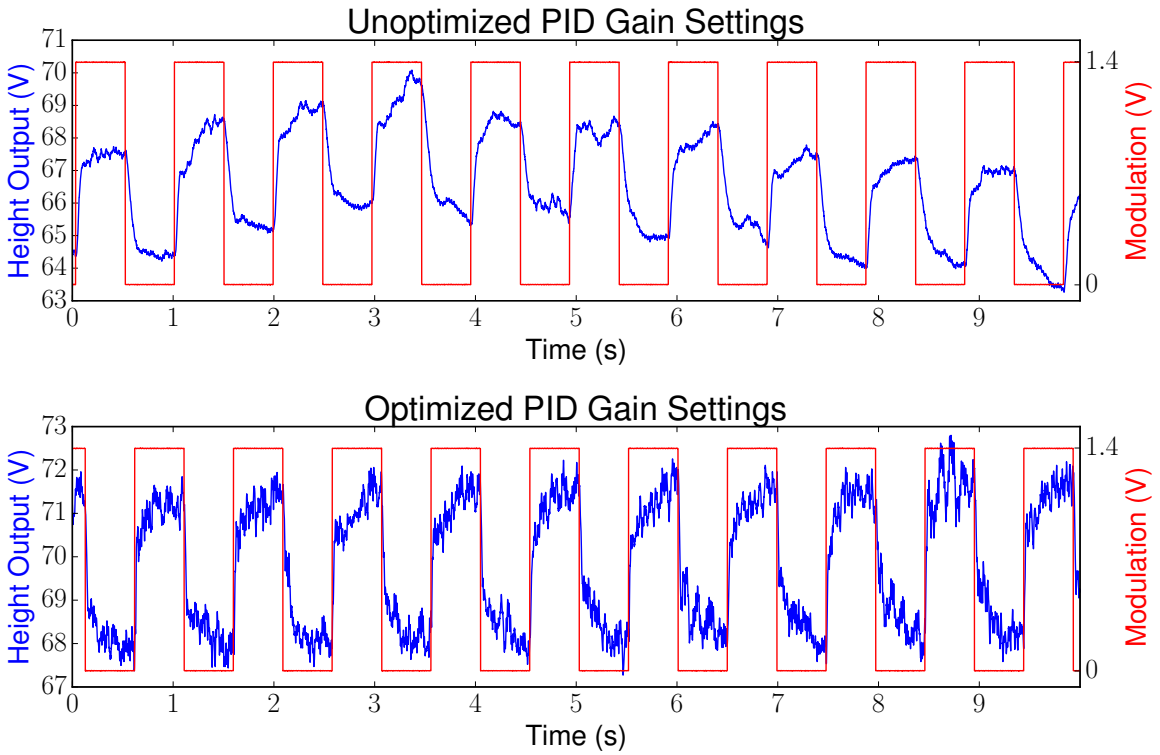

Figure 3.12: Top: Same plot as figure 3.9 for easy reference. Bottom: Plot with optimized PID gain settings. Note that the gradients of the height output signal are much steeper in the plot with optimized PID settings when the modulation signal changes. It is unknown why the signal continues to climb (drop) after the initial sharp increase (decrease). Uncertainty in height output signal is 0.005V, which is attributed to half the smallest digit of the reading.

Figure 3.12 shows an increased noise level in the height output signal. This is at-

tributed to the increase in the P and I gain settings. It also turned out that the system started to become noisy even before the optimization process began; something has triggered an increase level of noise between measurements of the two data sets in figure 3.12. The specific source of this increased noise level is unknown, but it could be due to the electronics and environmental factors.

3.3.2 Noise Reduction

In an effort to improve signal–to–noise ratio, data was collected for a longer period (e.g. 100s). The height output data was partitioned into blocks of one period each (e.g. 100 blocks for a 100s recording of a 1s period modulation). To account for the overall slow drift in the height signal output, each of the blocks is displaced vertically to have a mean of 0V. These processed blocks are averaged across to give a reduced noise picture of a single period of the height output. A *Python* script was written to perform this signal processing, and a sample of the code used is available in appendix A. Figure 3.13 shows a sample plot of the processed signal.

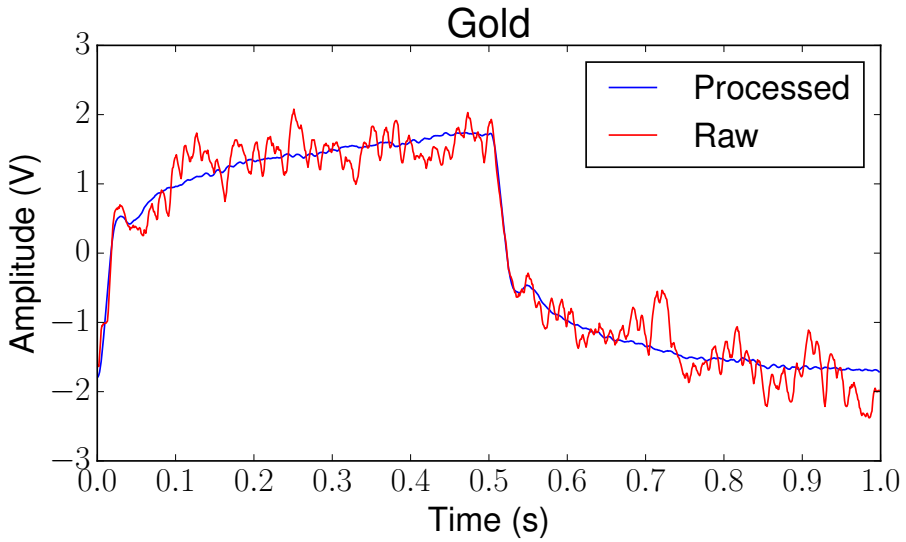

Figure 3.13: Plots of the processed signal and a sample of the raw signal for one period. Comparison of the processed and raw signals show a significant increase in the signal–to–noise ratio. Processed signal is the average of 100 blocks of one period each. Modulation is "on" for the first 0.5s and "off" for the remaining 0.5s.

Figure 3.13 shows a processed signal with much better signal–to–noise ratio than the raw signal, as can be seen from the much less fluctuations in the processed signal.

A similar analysis with the glass surface is shown in figure 3.14. Comparison between figures 3.13 and 3.14 shows little resemblance.

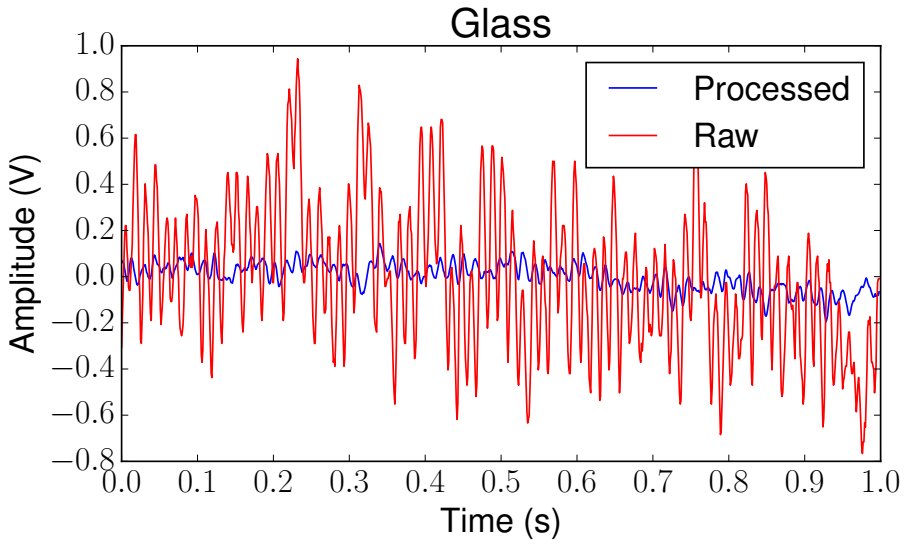

Figure 3.14: Plots of the processed signal and a sample of the raw signal for one period. Processed signal is the average of 50 blocks of one period each. No correlation with the modulation can be seen.

3.3.3 Analysis

It was hypothesized in the previous sections that the slow convergence nature of the curves was due to unoptimized PID gain settings. A low P gain setting would give us an exponential curve as the feedback system tries to match the input signal. Thermal expansion and contraction of the prism and gold film would also introduce an exponential curve.

Exponential fits using the least–squares method are performed on the processed signal for gold. The fits are performed with $y = ae^{bx} + c$ with a, b, and c constants to be determined. The fits are shown in figure 3.15.

It is quite apparent that the exponential fits do not agree well with the processed signal. The bad exponential fits indicate that neither of the aforementioned factors explain the exponential–like characteristic of the signal curve.

As an upper limit estimate on the contribution of thermal expansion, we assume that the gold film heats up to its melting point at about 1300K. Since the linear thermal expansion coefficient of gold is $14 \times 10^{-6}\,\mathrm{K}^{-1}$, and knowing that the gold film is at most 100nm thick, we have an expansion upper limit to be 1.4nm, which is too small to have caused a V_{pp} change over 4V; $V_{pp} = 10$V corresponds to about 1µm in the piezo. Hence, thermal expansion should not be the main contributing factor to the modulation that we see.

We observe overshoots in the processed signal, which manifest as concave bumps downwards (upwards) as the signal shoots up (down). The overshoot bumps can also be

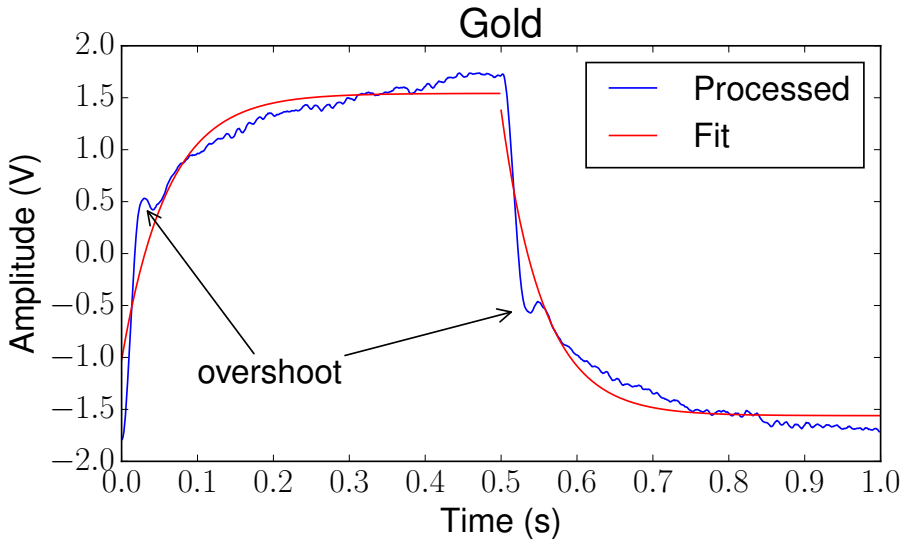

Figure 3.15: Plots of the processed signal and the exponential fits. Fits are optimized using the least–squares method on $y = ae^{bx} + c$. Fit parameters for the first curve are $a = -2.566 \pm 0.002$, $b = (-1.66192 \pm 0.00003) \times 10^{-2}$, and $c = 1.5421 \pm 0.0001$. Fit parameters for the second curve are $a = 2.939 \pm 0.002$, $b = (-1.81686 \pm 0.00002) \times 10^{-2}$, and $c = 1.5604 \pm 0.0001$. Overshoots in the signal manifest as concave bumps, which indicate that the P and I gain settings could not have been set to be too low.

seen in the raw signal in figure 3.13. This overshoot tells us that the P and I gain settings cannot have been set to be too low. Hence, this further rules out the possibility that the exponential–like curve is due to unoptimized PID gain settings. Further investigation is required to reveal the source of the exponential–like characteristic.

3.3.4 Nature of Exponential–like Curve

The power of the modulated laser beam was measured with a power meter, and the result is shown in figure 3.16.

Figure 3.16 shows no exponential–like curve in the power of the laser beam. Hence we can rule out the possibility that the exponential–like characteristic of the processed signal is due to the imperfect modulation of the incident laser beam. Furthermore, since overshoots in the power are only observed for the climb and not the descent, it is highly unlikely that this overshoot is responsible for the two overshooting bumps seen in the processed signal.

It now serves to take a step back to investigate whether the signal that we observe is in fact due to the evanescent fields or some other parasitic phenomenon.

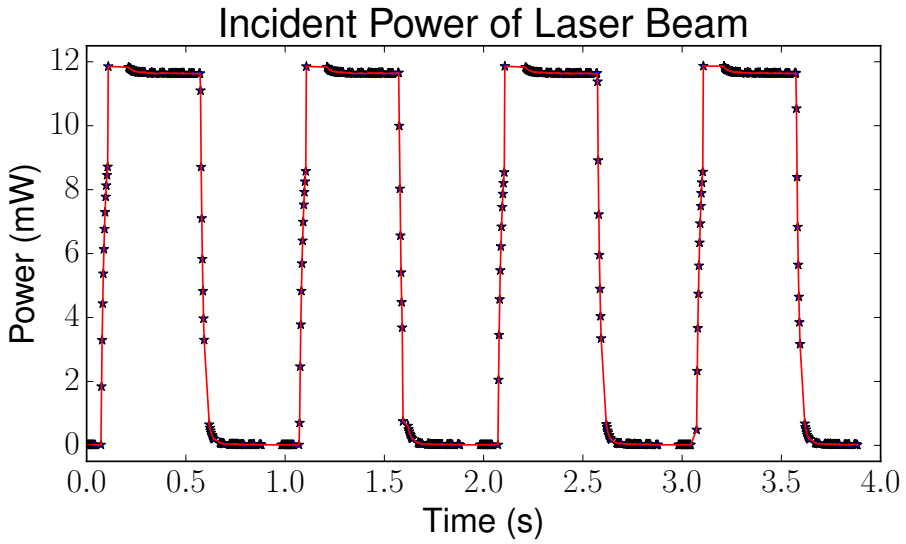

Figure 3.16: Plot of the power of the modulated laser beam against time. We see overshoots in the climb, but not in the drop. We also do not see continuous exponential–like growth (decay) after the initial climb (drop). Values measured are at most 1% away from the actual value; error bars are too small to be shown.

3.3.5 Nature of the Signals

Polarization Dependence

Plasmonic evanescent fields exhibit several characteristics. One of them is that surface plasmons can only be created by p–polarized light (as mentioned in section 1.2). As such, by changing the (linear) polarization of the incident laser beam, we hope to see some variations in the height output signal.

Firstly, a polarizing beam splitter (PBS) is placed in the path of the beam between M1 and the prism. A power meter is used to measure the power of the beam reflected by the PBS. Since the PBS reflects s–polarized light, the power meter measures the s–polarization component of the laser beam. This s–polarized light is in fact a p–polarized light for the prism due to the setup configuration. Hence from now on, the PBS s–polarized light shall be referred to as the p–polarized light for the prism without any ambiguity. The half wave plate (HWP) shown in figure 3.8 is rotated through a range of angles to rotate the polarization of the laser beam incident onto the prism. The power of the p–polarized light is mapped out against the angle of the HWP. For this measurement, the laser output was kept at a constant power. The result is shown in figure 3.17.

The PBS is then removed, and the 2 sets of height output signal data are collected for each of the HWP angle probed. For each set of data, 50s worth of data is collected for a total of 50 periods of square–wave modulation. These 50 periods are then processed to give one averaged processed signal like that performed in the previous pages. The

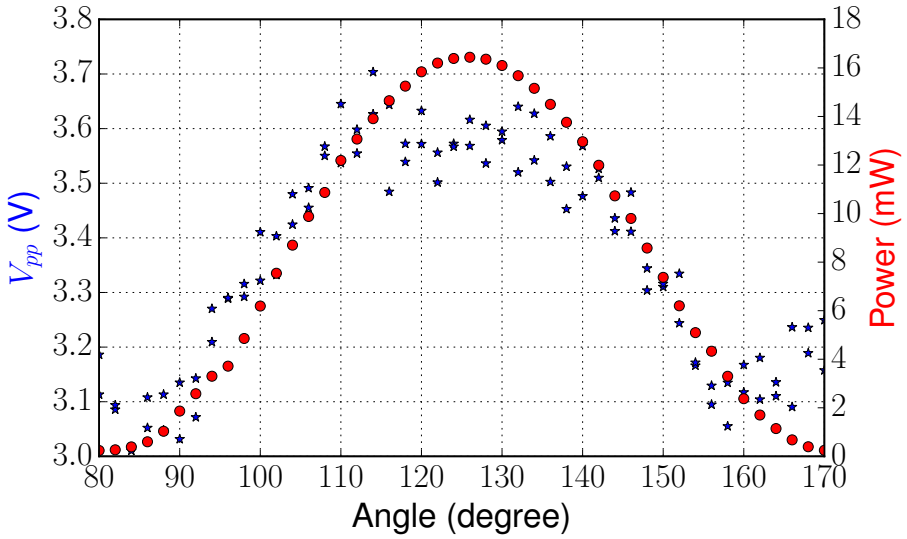

Figure 3.17: Red circles: Plot of measured p–polarization intensity against angle of HWP. Blue stars: Plot of max–min voltage of the processed height output signal; two sets of data are plotted together. Each of the angle measurements is precise down to 1°. The angles shown correspond to the angular markings on the HWP that was read out.

maximum and minimum voltages of the processed signals are found, and their difference is plotted as V_{pp} in figure 3.17.

An overall agreement in the general trends of the two plots can be seen in figure 3.17, which implies that there is detection of the plasmonic evanescent fields. However, we see that the plot for the V_{pp} of the processed height output is very scattered. Furthermore, we also see that the variation of V_{pp} is slightly more than 0.5V, which is small compared to the smallest V_{pp} at about 3V. This means that the modulation of the height output that is read out is not just due to the plasmonic evanescent fields, but also due to other complicating factors. Furthermore, a plasmonic enhancement factor of 14 would imply that the contribution of the plasmonic evanescent fields to V_{pp} in glass would be about 0.04V. Since this is much less than the fluctuations in the signal due to noise ($\sim$ 0.1V after processing), it explains why we see little resemblance of figure 3.14 to figure 3.13. A processed signal for glass taken with measurement taken for 1 hour (3600 periods of 1s period modulations) reveals V_{pp} of about 0.10V, which is slightly larger than expected. This plot is shown in figure 3.18.

Figure 3.18 is interesting in a few aspects: (i) the amplitude seems to be the inverted version of the modulation, i.e. "on" when modulation is "off" and vice versa; (ii) insofar as it the inverted version of the modulation, the slowly converging exponential–like curves still occur when the modulation is "on" and "off" respectively, agreeing with that of gold in figure 3.13. More will be discussed in the later sections of this thesis.

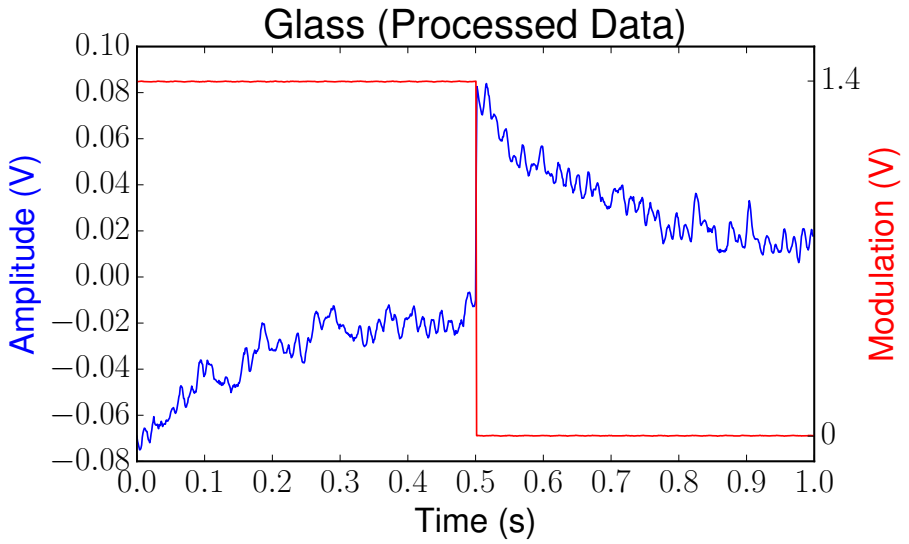

Figure 3.18: Plot of the processed signal for the detection of plasmonic evanescent field over glass. A total of 3600 periods are averaged across to increase signal–to–noise ratio for this plot.

Incident Angle Dependence

Another characteristic of the plasmonic evanescent fields is that the incident light and the surface plasmons couple most strongly at the resonant angle, resulting in intense evanescent fields at that angle, and an intensity width of only 0.5° for gold (Stehle et al., 2011). Hence, by varying the incident angle of the laser beam, we expect to see a sharp peak within 1° of the critical angle (Stehle et al., 2011). Figure 3.19 shows the results obtained from a scan of the incident angle, with the HWP at 125°, which is the angle of approximate maximum of V_{pp} in figure 3.17.

Figure 3.19 shows that there is a general decreasing trend as we move away from the critical angle. One of the reasons could be the change in size of the beam spot when the incident angle is changed. Images of the beam spot at each of the angles were taken, and the areas calculated with *Mathematica* are shown in figure 3.20. The series of images used for the calculation is available in figures B.1, B.2, and B.3 in appendix B.

As the incident angle increases, the prism wall cuts the Gaussian beam at an increasingly oblique angle. As such, the effective cross–sectional area of the beam increases with increasing incident angle. Moreover, since the incident angle is changed using the rail–mirror system with M1, as described in figure 3.8, the focal point of the focusing lens would have changed. A simple calculation shows that the Rayleigh length of the beam is about 2cm; M1 has moved slightly less than 1cm in the course of the angle adjustments, hence this would further increase the effective cross–sectional area of the beam in addition to the oblique angle effect. Since the total power of the beam must be the same regardless of the effective cross–sectional area, it goes to show that the intensity of the beam at the

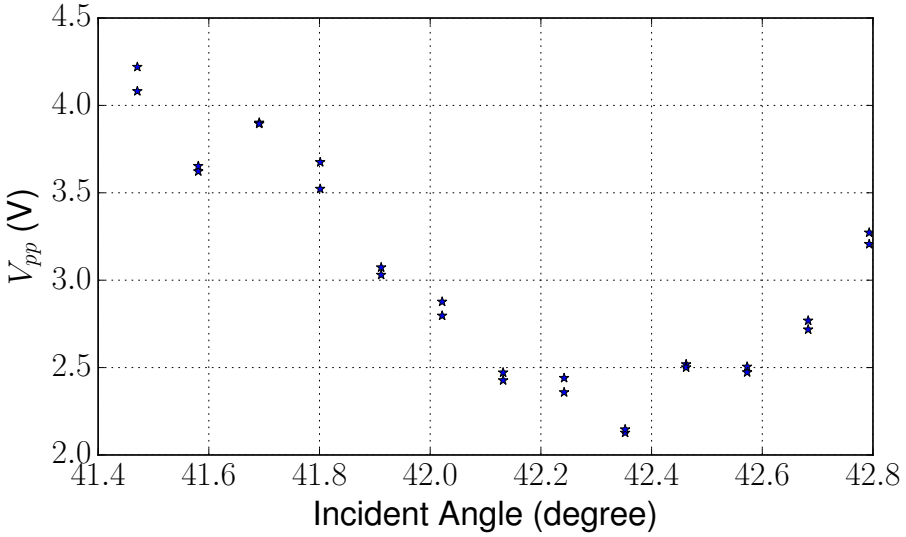

Figure 3.19: Plot of V_{pp} of the processed height output signal against the incident angle of the laser. Two sets of data are shown in the plot. There is no sharp peak with 0.5° width within 1° of the critical angle $\theta_c = 41.47°$. Angles plotted are precise to 0.05°.

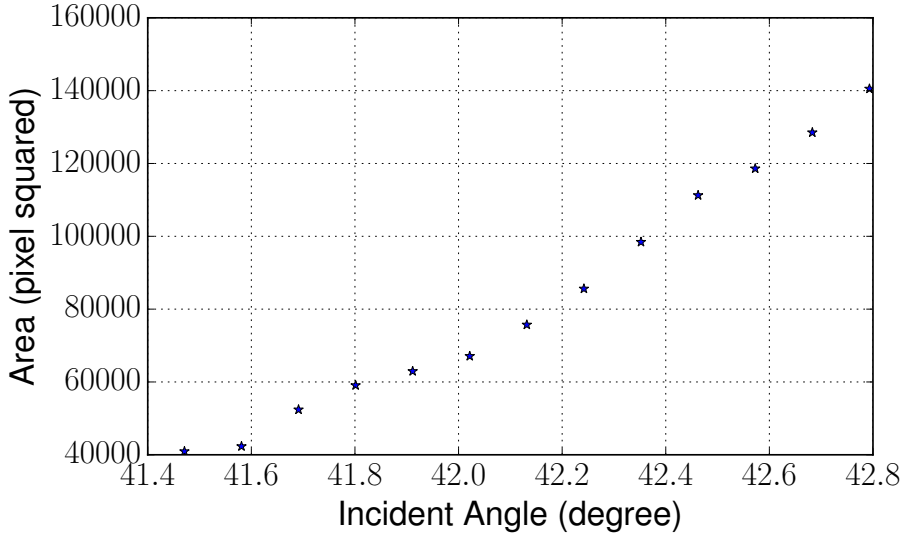

Figure 3.20: Area of the beam spot at varying incident beam angle by moving M1. There is an overall increase of a factor of 3.5 for the area as we move from 41.47° to 42.79°. Each of the areas is calculated by image processing using *Mathematica*. Angles plotted are precise to 0.05°.

prism wall decreases with increasing incident angle. This explains the general decreasing trend of V_{pp} in figure 3.19. The gradual increase of V_{pp} after the 42.4° mark could be due to other factors like scattering due to defects and impurities on the prism. After all, the fact that the beam spots can be seen on the outer wall of the prism despite total internal reflection happening on the inner wall beyond the critical angle suggests that there must be a certain level of defect and impurity on the prism wall, and on the gold film itself.

The deviations of the above results from those we expect of a plasmonic evanescent field prompts us to believe that there are many other factors involved in the apparent exponential–like curves we see in figure 3.15. Insofar as some signs of the plasmonic evanescent fields are detected in results shown in figure 3.17, we have little clue at this moment as to the other factors which contribute to the change in height output signal with the laser beam intensity modulation. However, we have eliminated the possibility of imperfect intensity modulation by inferring from the results in figure 3.16.

Observations from above suggests performing the same set of measurements on another prism for comparison of results. This is done in the next chapter.

3.4 Summary

In this chapter, we have described how the AFM feedback mechanism can be used to detect evanescent fields. We have managed construct a setup to detect evanescent fields successfully. We have also shown how the data obtained from the setup can be processed to increase the signal–to–noise ratio. The results obtained hint the presence of sources of unwanted contributions, possibly due to scattering from defects and dirt on the prism surface. This prompts us to perform the same set of experiments on a cleaner prism to see if the unwanted contributions are indeed due to the aforementioned reasons. This will be performed in the next chapter.

Chapter 4

Final Experimental Setup

In the previous chapter, we have seen how the AFM is much more superior than optical fibres as probes for the evanescent fields. The results from the previous chapter seem to indicate that light scattered by defects and dirt on the surface of the prism drowns the effects of the plasmonic evanescent fields. This chapter repeats the investigations from the previous chapter on a new and clean prism to show that the cleanliness of the prism is indeed very important for successful detection of plasmonic evanescent fields. This chapter will also introduce a simple addition to the experimental setup to aid in the field detection process.

4.1 Repeat of Analysis

A new prism with a 30nm thick gold film was fabricated. Once again, the gold film was fabricated on one half of the prism to allow for comparison of the evanescent fields with and without gold through simple translation of the prism. The prism used was made of fused silica, with refractive index $n = 1.46$.

With this new prism, similar measurements and analysis were performed with the previous section. For instance, a one hour measurement was performed on the prism without gold, and the processed result is shown in figure 4.1.

On comparison of microscope images of the glass surface for the old and new prisms, it is not hard to see that there is far less scattering from the glass surface of the new prism than the old (refer to figure 4.2). The new prism only has a few specks of scattering, whereas the old prism has a huge surface of scattered light.

The new prism analogue of figure 3.17 is shown in figure 4.3. The results are disturbing because there seems to be no correlation between V_{pp} of the processed signals and the intensity of the p–polarized incident beam. This suggests that the V_{pp}'s that we see are not due to the plasmonic evanescent fields, but are due to other effects like radiation pressure from scattered light instead. It also suggests that we are not at the angle where the incident beam couples with the surface plasmons most effectively.

A workaround to the aforementioned problems would be to introduce a sharply focused beam such that a wide range of $\mathbf{k}$ vectors are incident onto the tip. As such, it would be much easier to hit the tip at the resonant angle for the most effective coupling between

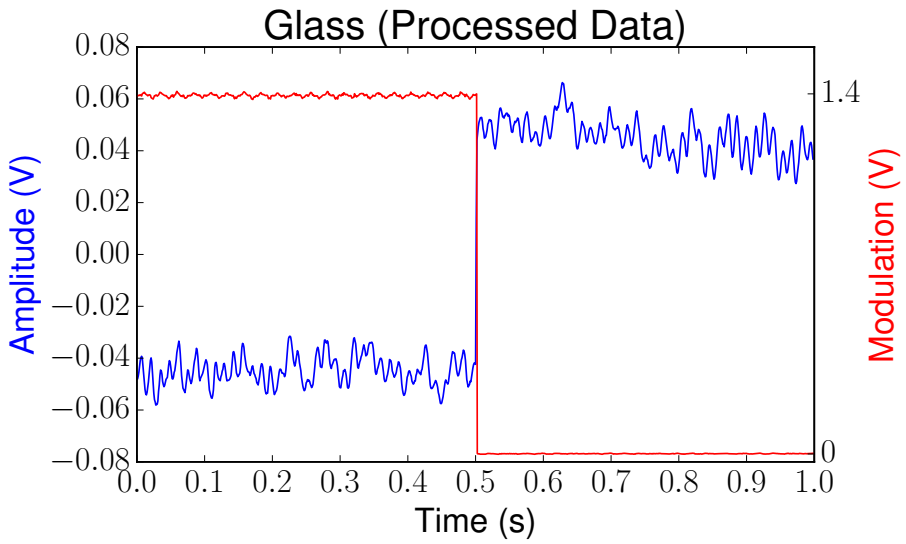

Figure 4.1: Analogue of figure 3.18. The exponential–like curves are gone. The amplitude is still the inverted form of the modulation signal. The wave–like squiggles in the modulation signal is due to cross–talk in the electronics of the data acquisition module.

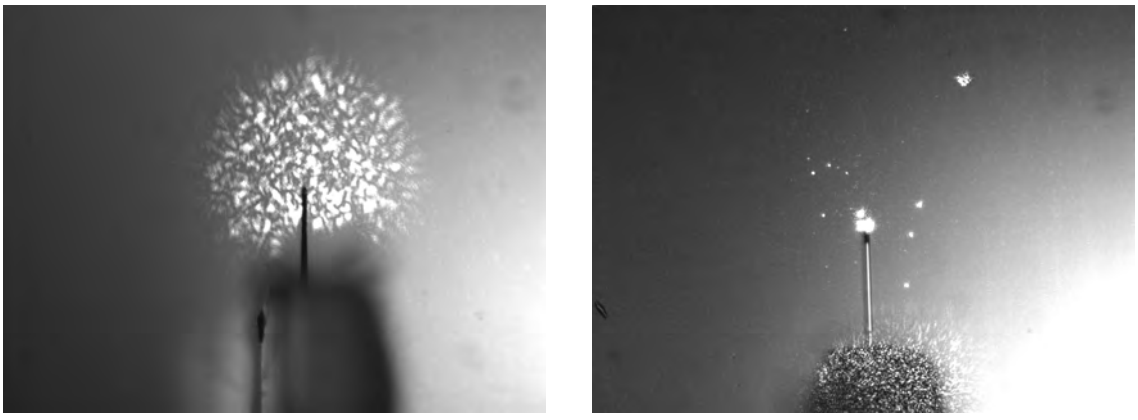

(a) Old Prism **(b)** New Prism

Figure 4.2: Comparison of the glass surface with laser beam on for the old and new prism. Much more scattering can be seen for the old prism than the new, which only has a few speckles. The bright spot on the lower right of the image for the new prism is due to imaging artefacts.

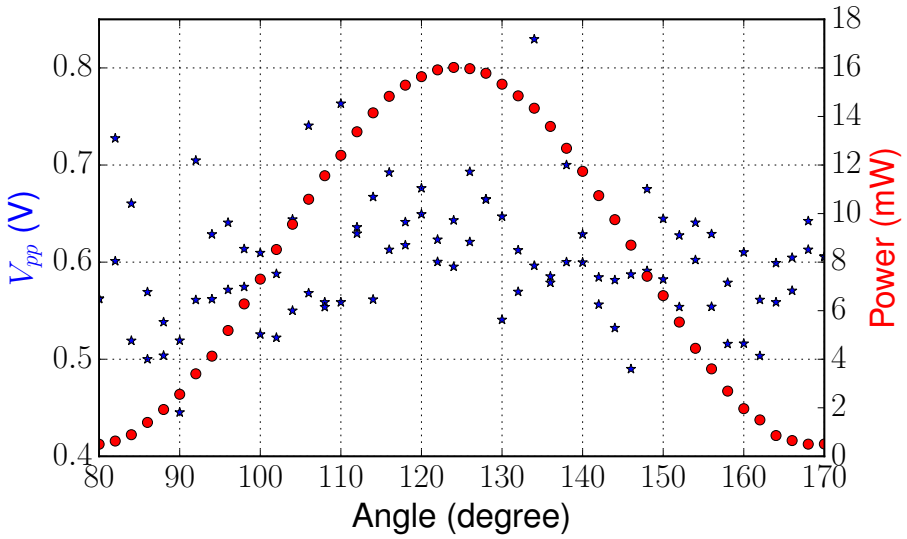

Figure 4.3: New prism analogue of figure 3.17, where the intensity of the p–polarized light is compared with V_{pp} of the processed height output signal of the AFM. Each of the angle measurements is precise down to 1°. The angles shown correspond to the angular markings on the HWP that was read out.

the incident beam and the surface plasmons to occur, but the trade–off is to have a smaller effective intensity to work with since the beam is spread out into different incident angles. To compensate for this, we increase the intensity of the laser. With the resonant angle on, it is hoped that the resulting plasmonic evanescent fields would induce a more significant force on the AFM than other factors like scattered light. A schematic diagram summarizing this paragraph is shown in figure 4.4.

Indeed, as figure 4.5 shows, the plot now shows the expected trend with after the aforementioned modifications to the setup were made.

We see from figure 4.5 that the contribution of the plasmonic evanescent fields to V_{pp} is still slightly above 0.5V like that in figure 3.17, but the contribution of external factors is now reduced to about 0.5V from the previous 3V for the old prism. This goes to show that scattering does induce a force on the AFM tip with comparable strength to that induced by the plasmonic evanescent fields.

Figure 4.6 compares processed signal for gold and glass. From this figure, we can clearly see the enhancement factor on the intensity of the evanescent fields due to the surface plasmons as V_{pp} for gold is about 10 times that for glass.

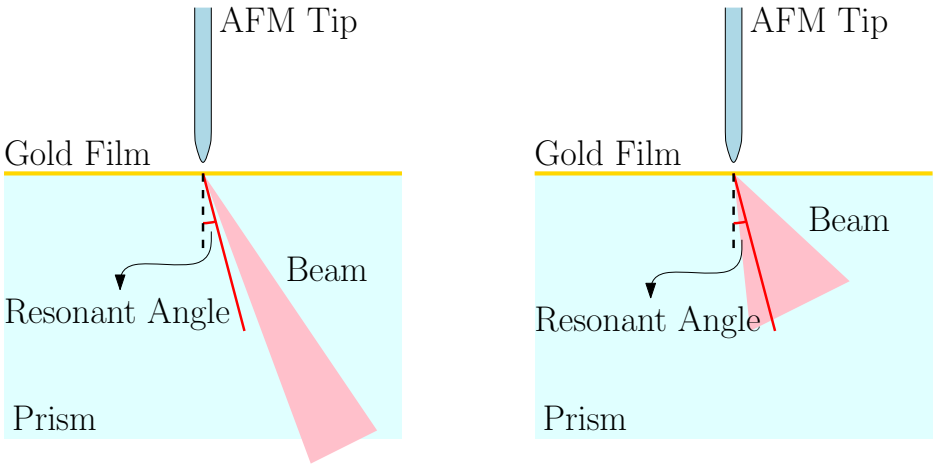

Focused with 30cm lens **Focused with 30mm lens**

Figure 4.4: Left: Using a 30cm lens to focus the incident beam; Resonant angle for the coupling is not included, which gives a plasmonic evanescent field with very small intensity. Right: Using a 30mm lens to focus the incident beam sharply; Resonant angle is included in the beam, which gives a more intense plasmonic evanescent field.

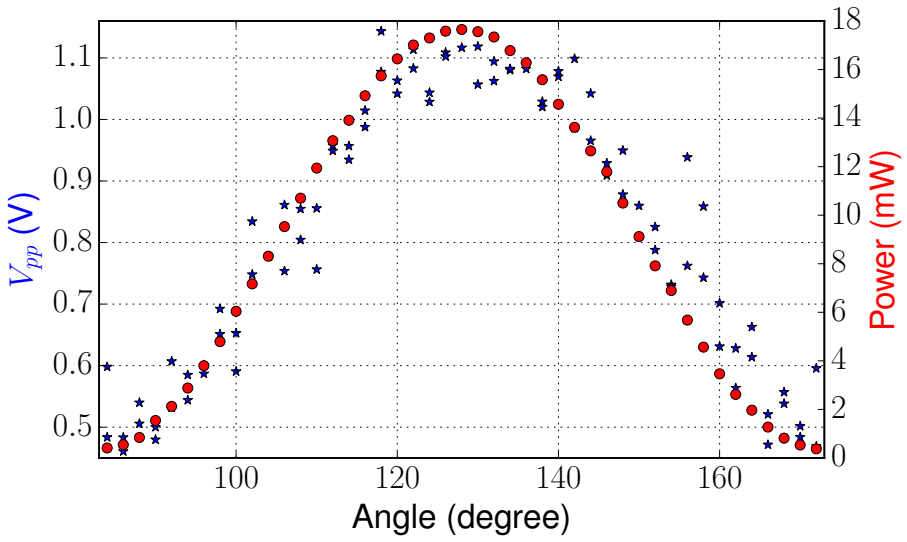

Figure 4.5: New prism analogue of figure 3.17 with the beam now sharply focused to give a range of incident angle. Star (blue) plot points are V_{pp} and circle (red) plot points are the power measurements of the p–polarized light. Each of the angle measurements is precise down to 1°. The angles shown correspond to the angular markings on the HWP that was read out.

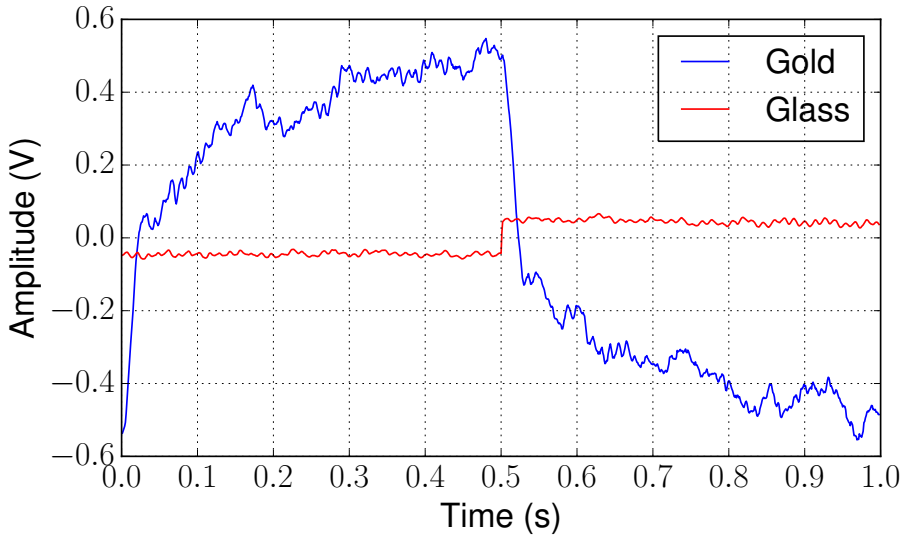

Figure 4.6: Plots of the processed signal for gold and glass. Processed signals for gold and glass are the average of 50 blocks and 3600 blocks of one period each respectively. Signal for glass is the same as that plotted in figure 4.1. Modulation is "on" for the first 0.5s and "off" for the remaining 0.5s. The amplitude for the signal for gold is about 10 times that for glass.

4.2 Outgoing Beam

In the previous section, we see hints of the plasmonic evanescent fields through the AFM detection system. Many of the observations can be explained by the required conditions for light–SP coupling to occur successfully: dependence of light–SP coupling strength on (i) polarization of incident light, and (ii) incident angle. In this section, we provide more experimental evidences to show that there is indeed light–SP coupling.

4.2.1 Resonant Angle

By projecting the beam coming out of the prism onto a screen, we see a distinct line with significantly low intensity then the other parts of the beam (refer to figure 4.7). This line corresponds to the part of the beam where the **k** vector happens to meet the resonant angle for the surface plasmon coupling. Since most of the beam with this **k** vector is coupled to the surface plasmons, we would expect a much weaker reflected beam as compared to other incident angles, which is precisely what we observe. We can also estimate the dark line width to be about 0.5° wide from figure 4.7d, which goes to show that the range of angles for the **k** vectors that we can work with for surface plasmon generation is in fact very narrow.

A closer look at the line depths in figure 4.7d tells us that at least two–thirds of the light intensity is coupled to the surface plasmon at resonant angle. This means that a lot

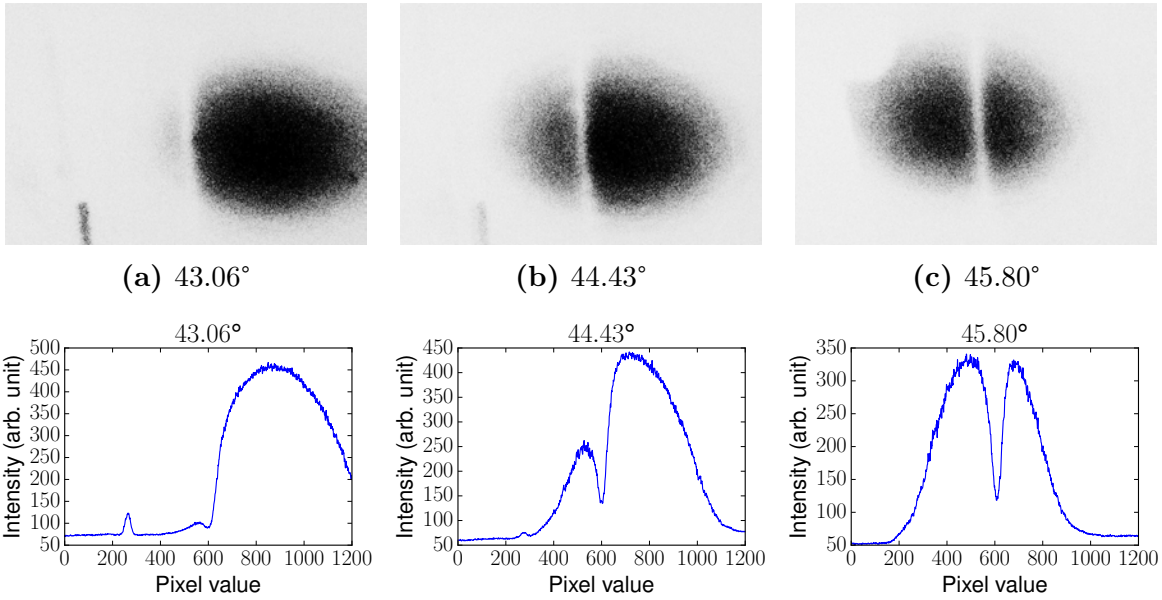

(a) 43.06° **(b)** 44.43° **(c)** 45.80°

(d) Plots of the intensity in arbitrary units across the row after adding contributions from all rows to reduce noise.

Figure 4.7: Images showing the beam coming out of the prism at various incident angles. Colour of images have been negated to save ink. A line of absorption corresponding to the resonant surface plasmon coupling angle can be easily seen. Beam spots seem elliptical because the camera was positioned at an angle from the screen. Each beam spot is about 5cm in diameter on the screen.

of the power can be coupled into the surface plasmons to form a strong plasmonic trap.

4.2.2 Light–SP Coupling

Figure 4.8 compares images of the beam after the prism for two cases: (i) when the beam reflects off the gold film in the inner wall of the prism, and (ii) when the beam reflects off fused silica without the gold film in the inner wall of the prism. It clearly shows that the line is indeed caused by surface plasmon coupling and not obstruction in the beam path.

As a check, the 3cm lens is switched back for the 30cm lens for a narrower band of **k** vectors. The beam spot after it reflects off the inner wall of the prism is captured on a screen for both reflection off gold and fused silica. The series of images is available in appendix C. The pixel values for each of these images are summed over with the background subtracted off to give us a plot shown in figure 4.9. The results agree with our expectations.

Figure 4.9 shows us a dip in the intensity of about 80% at the resonant angle. The power of the laser used in this experiment was about 15mW. This means that about 12mW of power was coupled into the gold film of just 30nm thick. Since all this power

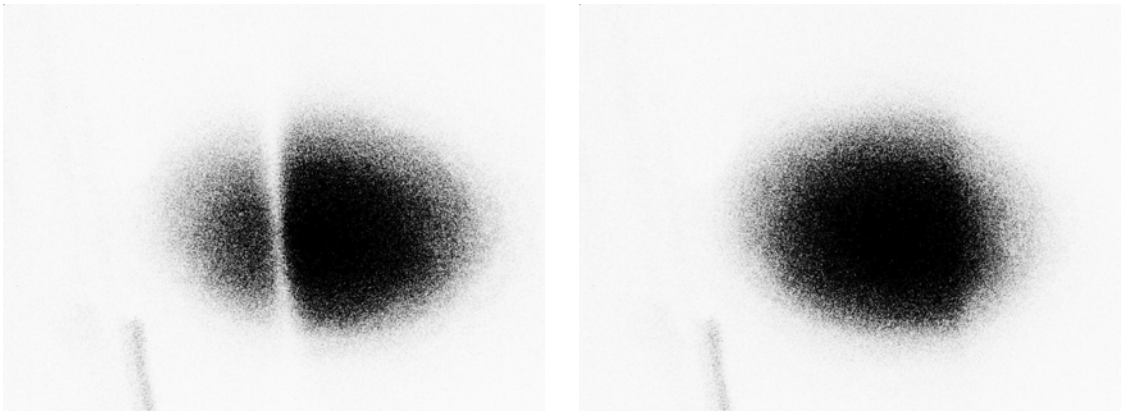

(a) Beam after reflecting off gold. **(b)** Beam after reflecting off fused silica.

Figure 4.8: Images of the beam after reflecting off the inner wall of the prism with and without the gold film. The incident angle is the same in both cases. The line is absent when the beam reflects off fused silica without the gold film. This clearly shows that the line is due to surface plasmon coupling in the gold film. Colours for images have been negated to save ink. Beam spots seem elliptical because the camera was positioned at an angle from the screen.

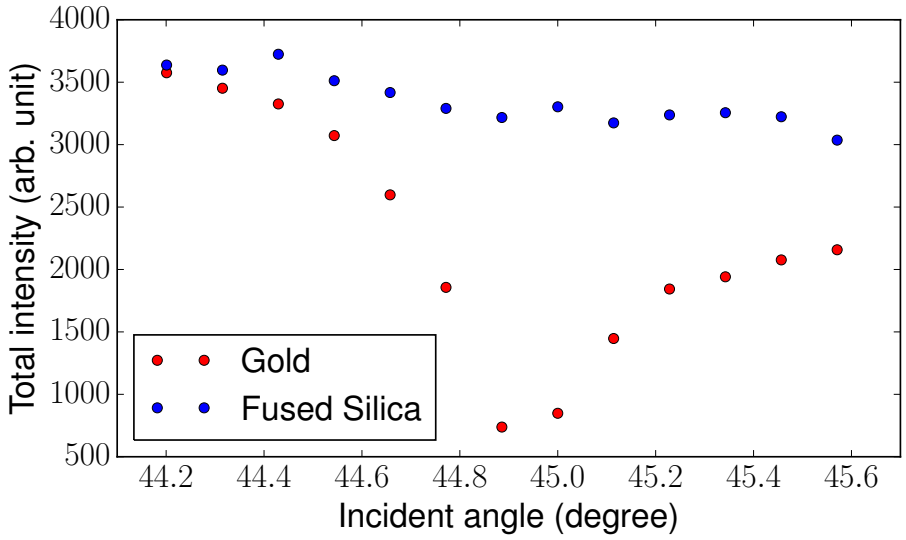

Figure 4.9: Summation of all the pixel values for each of the images of the reflected beam (refer to appendix C) taken at various incident angles. The background has been subtracted off from the plot values. The dip at around 44.9° for gold corresponds to the resonant coupling angle. The angles are precise to about 0.05°. Each beam spot is about 5cm in diameter on the screen.

must be concentrated in a volume within the decay lengths of the evanescent fields on both sides of the gold–air boundary (100nm for the air side and 5nm on the gold side), we see that the plasmonic evanescent field can be made very intense to give us a very strong trap situated very close to the surface.

4.2.3 AFM Tip Coupling

Since the AFM tip is a dielectric with a tip diameter of about 10nm, the tip may change the structure of the plasmonic evanescent fields as it probes the fields by modifying the boundary conditions for the Maxwell's equations. This is known as the back–action of the tip. Fortunately, we are now in a position to determine if the AFM tip introduces any significant back–action by comparing images of the reflected beam with and without the tip in contact with the surface.

A series of 1000 images were taken of the reflected beam on a screen after the beam reflects off the inner prism wall with the gold film with the AFM tip in contact with the surface in the centre of the beam. These images were stacked to give a noise–reduced image. The same is performed for the AFM tip retracted away from the surface. The difference between the two processed images was taken to see the effect of the AFM tip on the coupling between the incoming laser beam and the surface plasmons. The same process was repeated for the beam reflected off the inner prism wall without the gold film. The results are shown in figure 4.10.

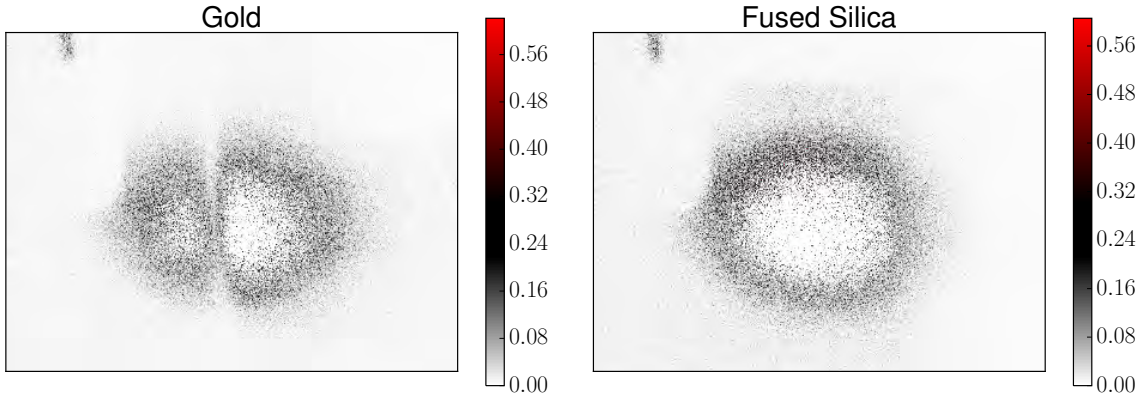

Figure 4.10: Resultant images of the difference (absolute) between the images of the beam with the AFM tip in contact with the surface and retracted away from the surface. Pixel values for the raw images range from 0 (no light) to 1 (saturated). The colour scheme has been chosen for maximum contrast; most of the pixel values lie within the black range. Each beam spot is about 5cm in diameter on the screen.

Figure 4.10 seems to suggest that the AFM tip does have an effect on the coupling between the incoming beam and the surface plasmons, i.e. back–action is introduced by the tip. However, closer inspection reveals that the back–action is occurring where we

do not expect them to. We would expect the tip to introduce back–action close to the tip, which is positioned in the centre of the beam, but we observe changes close to the rim of the beam spot. To make things worse, the beam spot on the inner wall of the prism has a diameter of about 150µm, while the AFM tip has a diameter of about 10nm. It makes little sense for this small tip to have little effect on its immediate surrounding, while having significant impact far away. This prompts us to look at the noise involved in the images used to create these processed images. Figure 4.11 shows the variance of the pixel values for the various configurations.

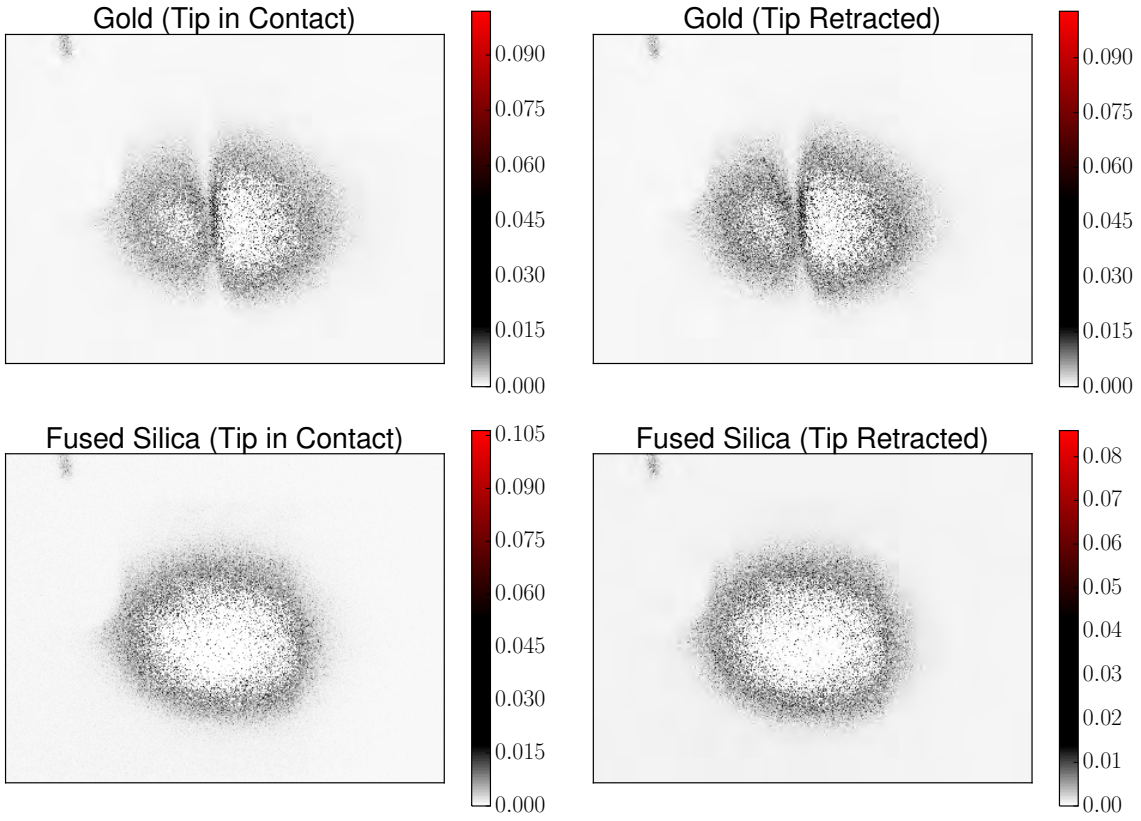

Figure 4.11: Images of the variances of the pixel values. Note that the regions with non–zero variances corresponds to those of figure 4.10. The colour scheme has been chosen for maximum contrast; most of the pixel values lie within the black range. Each beam spot is about 5cm in diameter on the screen.

Figure 4.11 tells us that the resultant images of figure 4.10 could be due to noise in the raw images instead of the back–action hypothesized. This would explain why the "back–action" does not occur where the tip is.

4.3 Discussion of Results

In the previous section, we have seen experimental evidences for the generation of surface plasmons in the form of (i) polarization dependence of incident light, and (ii) dependence of incident angle of the beam on the light–SP coupling strength. This gives us assurance that results obtained from the AFM can indeed be attributed to the plasmonic evanescent fields. At this stage, we can now propose a possible explanation for some peculiarities observed earlier.

4.3.1 Thermal Expansion

By comparing figure 4.1 with figure 3.18, we see significantly reduced exponential–like characteristic in the former from the latter. One of the possible sources of the exponential–like curves is thermal expansion of the prism. This inference comes from a few key observations:

1. There is much more scattering from the gold surface than from the glass/fused silica surface;

2. Slow convergence in the height output signal is concave downwards (upwards) when the modulation is "on" ("off");

3. Exponential–like characteristic is strongly suppressed in scans on new prism, which is much cleaner, and hence much less scattering, than the old one.

4. The time scale of this slow convergence is on the order of a second.

Defects within the gold film would convert surface plasmons into other forms of excitations including heat and scattered light. We have seen in the previous section that about 12mW of power has been coupled into the surface plasmons. This amount of energy cannot stay within the gold film forever, and it has to dissipate somewhere. One of the ways this energy can dissipate is through heat. We have shown with an upper limit estimate in the previous chapter that the thermal expansion of the gold film cannot be responsible for the magnitude of the signals that we see in the results. However, this heat can be transferred to the prism, which then heats up to give a more noticeable length expansion due to its size.

The distance between the clamp holding the prism and the surface of the prism is about 5mm. A ballpark estimate of the increase in temperature of the prism at the beam spot is about 10K. With the thermal expansion coefficient of BK7 to be $7.1 \times 10^{-6}\,\mathrm{K}^{-1}$, we get an expansion of about 0.07µm. This would correspond to a V_{pp} of about 0.7V, which is on the same order of magnitude as what we observe in figure 3.15.

This thermal expansion effect would be reduced when the laser beam reflects off glass or fused silica without the gold film as there are no surface plasmons to concentrate the energy. However, defects and dust on the surface of the prism would play a part in absorbing energy from the beam, and enhance the heating rate as compared to a clean prism with no defects. Hence, for the height output signals of the AFM tip on glass, we would expect to see the slow convergence on the old prism, and a reduced effect on the new one, which is precisely what the results show.

4.3.2 Sign of Height Output Signal

From the above analysis, it appears that an increasing height output signal corresponds to the AFM tip retracting away from the surface, while a decreasing height output signal implies that the AFM tip is moving closer to the surface. This would tie in well with the explanation for the exponential–like curves in the previous section.

It is then interesting to note that the modulation of the height output signal follows that of the modulation signal for gold, but inverted for glass and fused silica. This also holds for the old prism. This seems to suggest that the plasmonic evanescent fields induce a repulsive force on the AFM tip, while the evanescent fields from the glass and fused silica induce an attractive force instead. It is well known that the optical dipole force gives rise to a potential minimum where the intensity is greatest. Since the evanescent fields have highest intensity closest to the surface, it is no surprise to see an attractive force for the glass and fused silica. Volpe et al. (2006) hint at a repulsive potential by plasmonic evanescent fields when we go too close to the surface. This could explain the repulsive force the AFM tip experiences when the laser beam is modulated to be "on" on gold. It is important to not to confuse this repulsive force with the blue–detuned repulsive potential mentioned in the earlier sections which cold atoms experience, as this repulsive force is due to momentum transfer from the surface plasmon to the dielectric AFM tip. It is important to note, however, that the repulsive potential in the work of Volpe et al. (2006) is experienced by small dielectric spheres, which have different geometries from the AFM tip.

4.4 Summary

Comparison of the results of the old and new prism indeed shows that the probing of the plasmonic evanescent fields using the AFM tip is very sensitive to unwanted contributions like scattering from defects and dirt on the surface of the prism.

A simple modification to the setup gives a convenient method to check on the light–SP coupling. Using this method, we have shown that light–SP coupling is very sensitive to

the incident angle of the beam. The setup modification also opened new doors to the kind of information that can be extracted on the plasmonic evanescent fields. This would be greatly helpful for future works.

Chapter 5

Conclusion

We have discussed the theoretical motivation behind the creation of a plasmonic trap, and we have seen that the successful creation of a plasmonic trap requires p–polarized light and coupling at the resonant angle.

We have explored two different ways to probe the plasmonic evanescent fields. The optical fibre method was deemed inferior to the AFM tip method due to a variety reasons discussed like the lack of suitable surface–tip distance feedback system in the former. We have discussed how the AFM feedback system can be adapted to probe the plasmonic evanescent fields, and we have obtained positive results from it.

In the analysis of the results, we have made use of the polarization dependence of surface plasmon coupling to extract the effect of the plasmonic evanescent fields on the AFM tip amidst other contributing factors. We have seen that this is a weak effect which is comparable and easily drowned by other effects like radiation pressure from light scattering off the surface.

We have repeated the analysis on a new and clean prism with much less scattering and we saw that contribution from unwanted factors like scattering has been reduced. We have also seen the importance of coupling the light to the surface plasmon at the resonant angle for successful surface plasmon generation.

The project is still very much in the exploratory phase and much work has yet to be done. Progress seems promising and results are beginning to show. The setup is now ready for field characterization. Much information can be extracted with this setup. Future works could, for example, investigate the following:

1. The amount of power coupled into the gold film, and specifically into the surface plasmons with the use of power meters before and after the beam hits the prism. The latter can be done by using the polarization dependence of light–SP coupling.

2. It would be interesting to see what the maximum power that could be coupled into the surface plasmon is. This would give the upper limit to how strong the plasmonic trap can be.

3. A fully collimated beam with only one $\mathbf{k}$ vector can be used without the focusing 3cm and 30cm lenses. We would expect to see coupling only at one incident angle.

The intensity of the laser would have to be ramped up to make up for the loss of beam intensity without the focusing lenses.

4. It would be illuminating to perform an area map of the plasmonic evanescent fields for the whole beam spot instead of only at its centre as it is being done now.

5. Finally, all the above methodology can be used on prisms with various grating configurations.

The results of this project show that at least 60% of the light intensity can be coupled into the gold film as surface plasmons when the incident beam is at the resonant angle. Since most of this power is concentrated in a volume within the decay lengths of the evanescent fields on both sides of the gold–air boundary, we see that a lot of power can be pumped into this 105nm region of space. Equipped with very intense plasmonic evanescent fields, we would be able to create strong tight traps for cold atoms, and open doors to exciting physics.

Through this project, the stage has been laid for the characterization of plasmonic evanescent fields with various gold grating configurations. This would serve as a stepping stone to the creation of plasmonic traps for cold atoms using prisms coated with metallic structures.

Appendix A

Python Code for Processing Signals

The following is a sample code used to process the signals to increase the signal–to–noise ratio. A summary of the code is as follows:

1. Importing data
    - Take in data from files containing modulation signal and height output signal at various HWP angles.
2. Function to find trigger points
    - Using modulation signal as the trigger, find the trigger points.
3. Process chunks
    - Using the trigger points, chop the signals into chunks of one period each.
    - Subtract the mean of each chunk from itself to bring all chunks down to 0 mean. This is to account for the slow drift of the height output signals across time due to thermal drifts.
    - Take the average of all these processed chunks, and extract the maximum and minimum of elements from the averaged chunk. The difference between these two values will be known as V_{pp}.

Importing data

```
# Declaring empty arrays to store data for signals
h1=[]        # height output signal array
m1=[]        # modulation signal array

# Import data from files and store them in the arrays
for each in range(84,173,2):
    data=loadtxt("New2/"+str(each)+"_1.txt")

    height=[]
    modu=[]
```

```
    for i in range(len(data)/2):
        height.append(data[2*i])
        modu.append(data[2*i+1])

    h1.append([subsub for sub in height for subsub in sub])
    m1.append([subsub for sub in modu for subsub in sub])
```

Function to find trigger points

```
# Defines function to find trigger points
def getpoints(wf):
    el=0

    # Determine if modulation signal started as ''on'' or ''off''
    # ''On'': about 70 ; ''Off'': about 0
    if wf[0] > 30:
        pos=1        # ''on''
    else:
        pos=0        # ''off''

    # Declare empty arrays to store trigger points
    se=[]
    setemp=[]

    # Determine trigger points
    for each in wf:
        if each < 30 and pos == 1:
            setemp.append(el)
            pos=0
        if each > 30 and pos == 0:
            setemp.append(el)
            pos=1
        if size(setemp) == 2:
            se.append(setemp)
            setemp=[]
        el+=1

```

```
29      return se          # return trigger points
```

Processing chunks

```
1   # Declare empty array to store maximum and minimum values of averaged
2   #  processed chunks for different angles
3   y1=[]
4
5   # Process data
6   for k in range(len(range(84,131,2))):
7       startend=getpoints(m1[k])          # Find trigger points
8
9       cut=[]          # Declare empty array to store chunks
10
11      # Get chunks using trigger points and store in array
12      for each in range(len(startend)-1):
13          # Store chunk temporarily
14          temp=h1[k][startend[each][0]:startend[each][0]+999]
15
16          # Subtract mean of chunk from chunk
17          temp2=temp-(ones([1,len(temp)])*mean(temp))[0]
18          cut.append(temp2)
19
20      # Store maximum and minimum values of averaged chunks in array
21      y1.append(max(mean(cut,axis=0))-min(mean(cut,axis=0)))
```

Appendix B

Variation in Beam Spot Size

As M1 is adjusted to change the incident angle, the beam spot on the inner wall of the prism changes its size due to two factors: (i) the inner prism wall cuts the beam at an increasingly oblique angle when the incident angle increases, and (ii) the focal point is moved away from the inner prism wall due to the rail–mirror system involved (discussed in main text).

The series of figures shown here are the images showing the beam spots at various beam incident angles, and the area used in the calculation of the beam spot size using *Mathematica*.

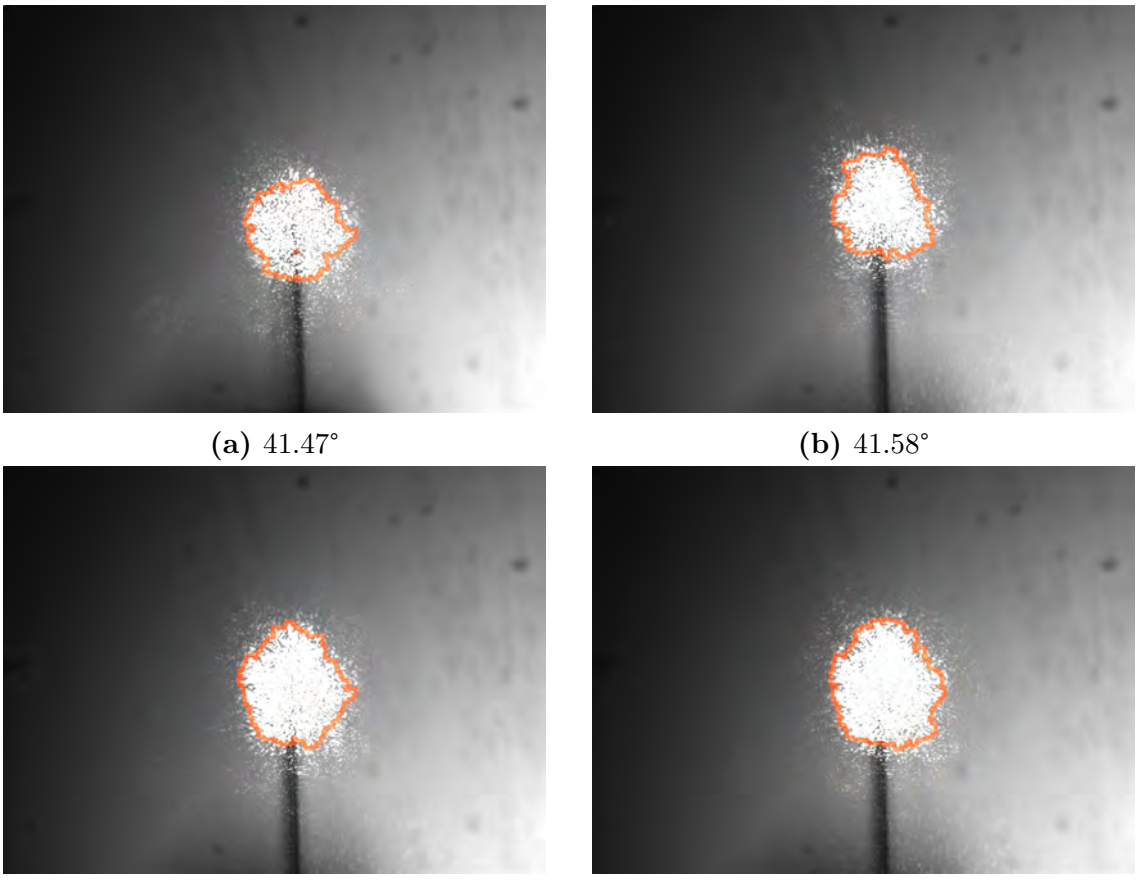

(a) 41.47° **(b)** 41.58°

(c) 41.69° **(d)** 41.8°

Figure B.1: Images show the size of the visible beam spot and the AFM tip. The area drawn out in orange marks the area of the beam spot used in the calculation.

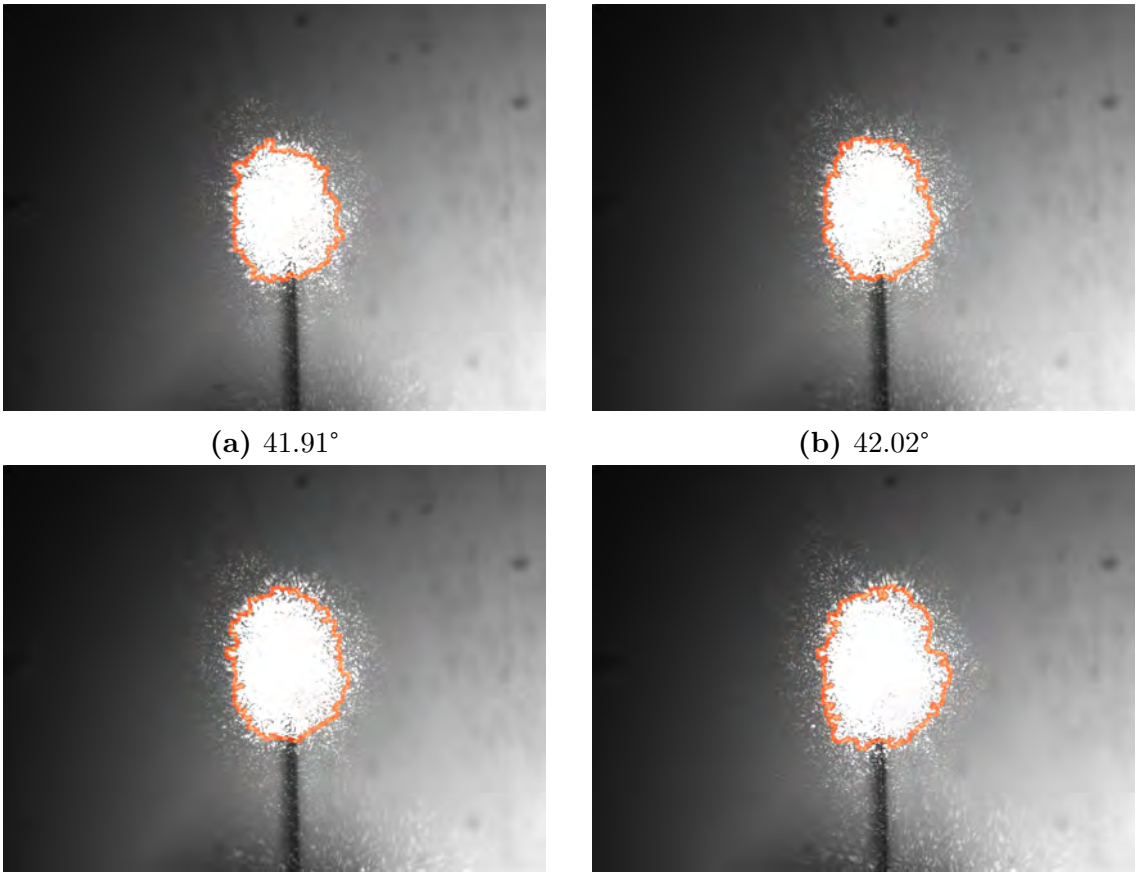

(a) 41.91° **(b)** 42.02°

(c) 42.13° **(d)** 42.24°

Figure B.2: Images show the size of the visible beam spot and the AFM tip. The area drawn out in orange marks the area of the beam spot used in the calculation. Continuation of figure B.1.

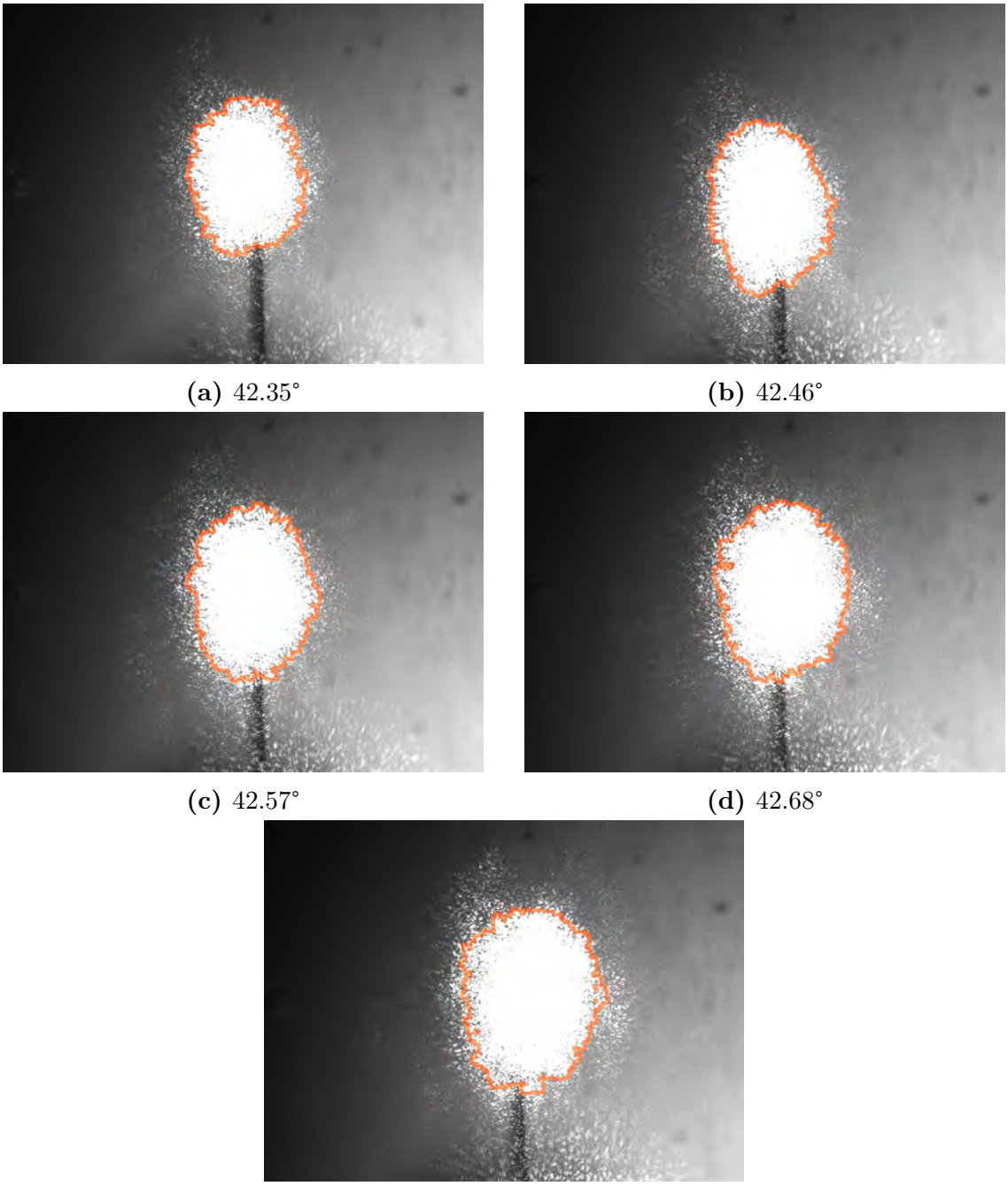

(a) 42.35°

(b) 42.46°

(c) 42.57°

(d) 42.68°

(e) 42.79°

Figure B.3: Images show the size of the visible beam spot and the AFM tip. The area drawn out in orange marks the area of the beam spot used in the calculation. Continuation of figure B.2.

Appendix C

SP Resonant Coupling Angle

Using a 30cm lens to focus the beam onto the inner wall of the prism introduces only a narrow range of incident angles. Images of the beam coming out of the prism were captured on a screen for a range of incident angles for the beam reflected off gold and fused silica. These images are placed side by side for comparison. Of note is figure C.2d where the beam covers the resonant angle, and most of the beam is coupled to the surface plasmon, which results in a diminished reflected intensity.

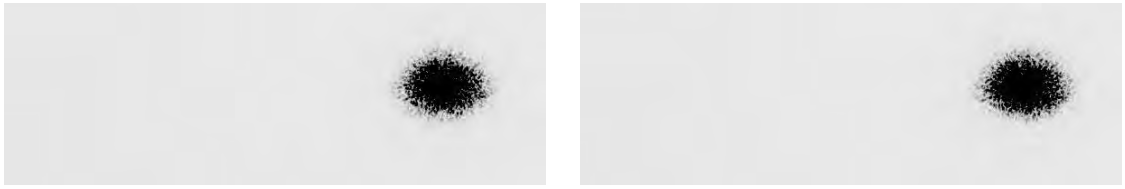

(a) 44.20°

(b) 44.32°

(c) 44.43°

Figure C.1: Left: Image of beam after it reflects off gold. Right: Image of beam after it reflects of fused silica. Images on the left are identical to images on the right except for angles near the surface plasmon resonant coupling angle. Colours of images are negated to save ink. Images are split into multiple figures due to page restriction. Angles stated above are values for the incident angle.

(a) 44.54°

(b) 44.66°

(c) 44.77°

(d) 44.89°

(e) 45.00°

(f) 45.11°

Figure C.2: Left: Image of beam after it reflects off gold. Right: Image of beam after it reflects of fused silica. Images on the left are identical to images on the right except for angles near the surface plasmon resonant coupling angle. Colours of images are negated to save ink. Images are split into multiple figures due to page restriction. Angles stated above are values for the incident angle.

(a) 45.23°

(b) 45.34°

(c) 45.46°

(d) 45.57°

Figure C.3: Left: Image of beam after it reflects off gold. Right: Image of beam after it reflects of fused silica. Images on the left are identical to images on the right except for angles near the surface plasmon resonant coupling angle. Colours of images are negated to save ink. Images are split into multiple figures due to page restriction. Angles stated above are values for the incident angle.

Bibliography

R. Grimm, M. Weidemüller, and Y. B. Ovchinnikov, Advances in atomic, molecular, and optical physics **42**, 95 (2000).

E. Vetsch, D. Reitz, G. Sagué, R. Schmidt, S. Dawkins, and A. Rauschenbeutel, Physical review letters **104**, 203603 (2010).

M. Righini, G. Volpe, C. Girard, D. Petrov, and R. Quidant, Physical review letters **100**, 186804 (2008).

C. Stehle, H. Bender, C. Zimmermann, D. Kern, M. Fleischer, and S. Slama, Nature Photonics **5**, 494 (2011).

C. Stehle, C. Zimmermann, and S. Slama, arXiv preprint arXiv:1311.7495 (2013).

S. Kawata and T. Sugiura, Optics letters **17**, 772 (1992).

H. Raether, *Surface plasmons on smooth and rough surfaces and on gratings*, no. v. 111 in Springer tracts in modern physics (Springer, 1988), ISBN 9783540173632.

P. B. Johnson and R.-W. Christy, Physical Review B **6**, 4370 (1972).

O. Marti, H. Bielefeldt, B. Hecht, S. Herminghaus, P. Leiderer, and J. Mlynek, Optics communications **96**, 225 (1993).

G. Binnig, C. F. Quate, and C. Gerber, Physical review letters **56**, 930 (1986).

H.-J. Butt, B. Cappella, and M. Kappl, Surface science reports **59**, 1 (2005).

Nanonics, *MultiView 2000 User Guide for the Integra Controller with NWS software*, Nanonics Imaging Ltd. (2010).

G. Volpe, R. Quidant, G. Badenes, and D. Petrov, Physical review letters **96**, 238101 (2006).